

Modal stability theory

Matthew P. Juniper

Cambridge University
Engineering Department
Trumpington Street, Cambridge, CB2 1PZ
UK
Email: mpj1001@cam.ac.uk

Ardeshir Hanifi

Swedish Defence Research Agency
FOI, SE-164 90, Stockholm
Sweden
Linné FLOW Centre, Mechanics, KTH
SE-100 44, Stockholm
Sweden
Email: ardeshir.hanifi@foi.se

Vassilios Theofilis

Universidad Politécnica de Madrid
School of Aeronautics
Plaza Cardenal Cisneros 3
E-28040 Madrid, Spain
Email: vassilis@aero.upm.es

ABSTRACT

This article contains a review of modal stability theory. It covers local stability analysis of parallel flows including temporal stability, spatial stability, phase velocity, group velocity, spatio-temporal stability, the linearized Navier–Stokes equations, the Orr–Sommerfeld equation, the Rayleigh equation, the Briggs–Bers criterion, Poiseuille flow, free shear flows, and secondary modal instability. It also covers the Parabolized Stability Equation (PSE), temporal and spatial bi-global theory, 2D eigenvalue problems, 3D eigenvalue problems, spectral collocation methods, and other numerical solution methods. Computer codes are provided for tutorials described in the article. These tutorials cover the main topics of the article and can be adapted to form the basis of research codes.

1 Introduction

Traditionally, the instability of flows to small amplitude perturbations has been analysed using the *modal* approach. Given an operator that describes the evolution of small perturbations, this approach considers the temporal or spatial development of individual eigenmodes of that operator. The resulting linear stability theory (LST) relies on the decomposition of any flow quantity \mathbf{q} into a steady part $\bar{\mathbf{q}}$, which is usually called the *basic state* or *base flow*^{*}, and an unsteady part $\tilde{\mathbf{q}}$

$$\mathbf{q}(\mathbf{x}, t) = \bar{\mathbf{q}}(\mathbf{x}) + \varepsilon \tilde{\mathbf{q}}(\mathbf{x}, t), \quad (1)$$

where \mathbf{x} is the space coordinate vector, t is time and $\varepsilon \ll 1$ is a small amplitude. Substituting this ansatz into the Navier–Stokes equations, subtracting the equations for the steady flow, and dropping the terms

^{*}not to be confused with the term *mean* flow/state, which is reserved for time and/or space-averaged turbulent flow

in ε^2 yields the linearised perturbation equations, referred to as the *Linearized Navier–Stokes Equations - LNSE*. In incompressible flow, the LNSE take the form

$$\frac{\partial \tilde{\mathbf{u}}}{\partial t} + \tilde{\mathbf{u}} \cdot \nabla \bar{\mathbf{u}} + \bar{\mathbf{u}} \cdot \nabla \tilde{\mathbf{u}} = -\nabla \tilde{p} + \frac{1}{Re} \nabla^2 \tilde{\mathbf{u}}, \quad (2)$$

$$\nabla \cdot \tilde{\mathbf{u}} = 0. \quad (3)$$

Once a basic state $\bar{\mathbf{q}}$ has been provided, the LNSE may be solved as an initial-boundary-value problem (IBVP) and are valid for any small amplitude perturbation, both *modal* (to be defined shortly) and *non-modal*, discussed in the article by Schmid and Brandt [1] in this volume.

It should be mentioned that the choice/computation of the basic state $\bar{\mathbf{q}}$ around which the linearization is performed is not always an easy task. This is especially cumbersome for flows that are globally/absolutely unstable. The choices are usually either the steady solution of the Navier–Stokes equations or the time average of the flow field. A classical case is the flow behind a cylinder at moderate to high Reynolds numbers, for which results based on the steady solution have the wrong frequency of unstable modes, while results based on the time-averaged flow have similar frequencies to those observed experimentally [2]. The main problem in such cases is that it is difficult to predict the characteristics of instability waves because the time average of the flow can be obtained only when the flow field is measured/computed with perturbations being present. For examples of such flow cases see Sipp and Lebedev [3]. A numerical approach for computation of the steady state for strongly unstable flows, when using time-stepping solvers, is so-called *Selective Frequency Damping* (Åkervik et al. [4]). Here, the amplitude of the solution corresponding to the strong instability is damped through application of an appropriate forcing. Alternatively, Newton methods may be used to obtain the steady state solution. In order to assess whether a given basic state is stable or unstable to an arbitrary small-amplitude perturbation, one can either solve the LNSE or perform a Direct Numerical Simulation of the full nonlinear equations of motion. Both of these are very computationally expensive, however, so this article describes some cheaper alternatives, which involve linear stability theory (LST). In the absence of experimental results to compare with those from LST, numerical solutions of the LNSE or a DNS of small-amplitude perturbations superposed upon a given basic state should be obtained [5–7]. This checks the LST results and, in the case of DNS, also shows how nonlinear perturbations develop. Further discussion of this point may be found in section 4.4.

Mathematical expediency and the lack of sufficient computing power during the last century dictated drastic simplifications to the form of perturbations, $\tilde{\mathbf{q}}(\mathbf{x}, t)$ in (1) that were studied by LST. These limited LST to flows that are homogeneous in two out of three spatial directions. Classic examples include free and confined shear flows, such as mixing layer flows and planar channel flows. In these cases, the perturbations are expanded in terms of their Laplace transform in time and Fourier transform in one or two spatial dimensions. The stability is determined separately for each mode, giving rise to the term *modal* LST. Explicitly, the perturbation vector $\tilde{\mathbf{q}}$ in (1) takes the form

$$\tilde{\mathbf{q}} = \hat{\mathbf{q}} e^{i\Theta}, \quad (4)$$

where $\hat{\mathbf{q}}$ and Θ are the *amplitude* and *phase* functions of the linear perturbations, respectively.

In recent decades, efficient algorithms for the solution of multi-dimensional eigenvalue problems, as well as the wide availability of appropriate computing hardware, have allowed modal stability analysis to be performed on any laminar steady flow. When starting a new flow stability problem, the first consideration is the number of homogeneous directions in the basic state. Table 1 shows the underlying assumptions about the homogeneity of the basic state $\bar{\mathbf{q}}$, the dimensionality of the perturbations $\tilde{\mathbf{q}}$, and the resulting framework and associated nomenclature for LST.

	Denomination	Basic State Assumption	Amplitude Function	Phase Function Θ	
<i>Global</i>	TriGlobal	-	$\bar{\mathbf{q}}(x_1, x_2, x_3)$	$\hat{\mathbf{q}}(x_1, x_2, x_3)$	ωt
	PSE-3D	$\partial_1 \bar{\mathbf{q}} \ll \partial_2 \bar{\mathbf{q}}, \partial_3 \bar{\mathbf{q}}$	$\bar{\mathbf{q}}(x_1^*, x_2, x_3)$	$\hat{\mathbf{q}}(x_1^*, x_2, x_3)$	$\int^{x_1} \alpha(x') dx' - \omega t$
	BiGlobal	$\partial_1 \bar{\mathbf{q}} = 0$	$\bar{\mathbf{q}}(x_2, x_3)$	$\hat{\mathbf{q}}(x_2, x_3)$	$\alpha x_1 - \omega t$
<i>Non-Local</i>	PSE	$\partial_1 \bar{\mathbf{q}} \ll \partial_2 \bar{\mathbf{q}}; \partial_3 \bar{\mathbf{q}} = 0$	$\bar{\mathbf{q}}(x_1^*, x_2)$	$\hat{\mathbf{q}}(x_1^*, x_2)$	$\int^{x_1} \alpha(x') dx' + \beta x_3 - \omega t$
<i>Local</i>	OSE	$\partial_1 \bar{\mathbf{q}} = \partial_3 \bar{\mathbf{q}} = 0$	$\bar{\mathbf{q}}(x_2)$	$\hat{\mathbf{q}}(x_2)$	$\alpha x_1 + \beta x_3 - \omega t$

Table 1. Classification of modal Linear Stability Theories

At the strongest level of approximation, the basic state is considered homogeneous along two spatial directions and then the *parallel flow* approximation is made. In this approximation, the wall-normal velocity component and the streamwise derivatives of the mean flow are assumed to be negligible. One can then assume that [8–10]

$$\tilde{\mathbf{q}}(\mathbf{x}, t) = \hat{\mathbf{q}}(x_2) \exp\{i(\alpha x_1 + \beta x_3 - \omega t)\}. \quad (5)$$

Inserting the above ansatz into the perturbation equations (2, 3) leads to a one-dimensional generalized eigenvalue problem. Details are given in section 2.5. In the past century, LST was performed mainly on flows that satisfied this ansatz, either exactly (e.g. plane- or Hagen–Poiseuille flow) or approximately (e.g. the flat plate boundary layer).

When a flow varies slowly in one spatial direction, say x_1 , a WKBJ type of approach can be considered. The ansatz (5) can be re-formulated as

$$\tilde{\mathbf{q}}(\mathbf{x}, t) = \hat{\mathbf{q}}(x_1, x_2) \exp\left\{i \left[\int_{x_0}^{x_1} \alpha(x') dx' + \beta x_3 - \omega t \right] \right\}, \quad (6)$$

where streamwise variations of $\hat{\mathbf{q}}(x_1, x_2)$ and $\alpha(x)$ scale with Re^{-1} . This approximation results in a set of local equations such as (5), which can either be solved as 1D eigenvalue problems in a local stability analysis, section 2.5, or as a set of *Parabolized Stability Equations, (PSE)* [11], which will be discussed in section 4. The PSE is typically used to study instability in the important class of the (weakly-nonparallel) flat plate boundary layer flow, and can also account for curvature effects and non-linear perturbation development.

When the basic flow is strongly dependent on two spatial directions but homogeneous in the third, the following ansatz is appropriate

$$\tilde{\mathbf{q}}(\mathbf{x}, t) = \hat{\mathbf{q}}(x_2, x_3) \exp\{i(\alpha x_1 - \omega t)\}, \quad (7)$$

substitution of which into the LNSE results in a two-dimensional (so-called *BiGlobal*) eigenvalue problem; this will be discussed in section 5. BiGlobal LST can be used to analyse the stability of flows such as that over a cylinder, a step, or an open cavity, all of which may be homogeneous along the span. It can also be used to study axially-homogeneous flows in ducts of arbitrary cross section, isolated model vortices, and systems of infinitely-long model vortices.

When the base state depends strongly on two spatial directions and weakly on the third, an extension of the classic PSE concept, labelled PSE-3D, may be used following the ansatz

$$\tilde{\mathbf{q}}(\mathbf{x}, t) = \hat{\mathbf{q}}(x_1, x_2, x_3) \exp \left\{ i \left[\int_{x_0}^{x_1} \alpha(x') dx' - \omega t \right] \right\}. \quad (8)$$

By contrast to the PSE, which advances a perturbation with a one-dimensional perturbation depending on x_2 along the streamwise spatial direction x_1 , PSE-3D advances a two-dimensional perturbation defined on the plane (x_2, x_3) along the direction normal to the plane x_1 .

Finally, when no homogeneity assumption is permissible on the basic flow, one has to resort to addressing the three-dimensional eigenvalue problem resulting from substituting

$$\tilde{\mathbf{q}}(\mathbf{x}, t) = \hat{\mathbf{q}}(x_1, x_2, x_3) \exp\{i\omega t\} \quad (9)$$

into the LNSE. The related context is referred to as *TriGlobal* LST. The areas of BiGlobal, PSE-3D and TriGlobal modal linear stability theories, collectively referred to as *global* LST, are rapidly expanding; see [12] for a recent review. The present article presents a common theoretical foundation for all of the *local*, *non-local* and *global* frameworks shown in Table 1.

Section 2 introduces local stability analysis and terminology such as temporal instability, spatial instability, convective instability, and absolute instability. The first tutorials in this section focus on flows with piecewise-linear and top hat velocity profiles, whose governing equations can be solved without numerical methods. Later tutorials focus on parabolic and tanh velocity profiles, whose stability requires the use of simple numerical methods, which are detailed in the appendix. Section 3 introduces secondary instabilities, which occur on top of the primary instabilities investigated in section 2. Section 4 introduces the Parabolized Stability Equations, which allow non-local and nonlinear effects to be included in slowly-developing flows. Section 5 introduces two-dimensional problems in linear stability. Section 6 describes numerical solution methods for all types of linear stability problems.

2 Local stability analysis

Local stability analysis concerns either parallel flows (5) or, via the WKBJ approach, flows that vary slowly in one spatial direction (6). Many of the concepts in local stability analysis, such as convective and absolute instability, are used to provide physical insight into the behaviour found in global stability analysis. In globally unstable flows, local analysis is therefore increasingly used as a diagnostic tool, rather than as a predictive tool. In globally stable flows, however, local stability analysis can be more useful than global stability analysis, as described in section 5. The basic concepts of local stability analysis are introduced in this section. These are then applied to a simple class of unstable flows in the Matlab tutorials.

2.1 Temporal local stability

In temporal linear stability analysis, the quantities α and β appearing in (5-7) are real wavenumber parameters, related to periodicity wavelengths, L_{x_1} and L_{x_3} , along the x_1 and x_3 directions, respectively, by $\alpha = 2\pi/L_{x_1}$ and $\beta = 2\pi/L_{x_3}$. The eigenvalue sought is ω , which is in general complex. This approach has been used for well over a century and can be found in many classic texts [13, 14]. The equivalent formulation of linear two-dimensional waves

$$\tilde{\mathbf{q}} = \hat{\mathbf{q}}(x_2) e^{i\alpha(x_1 - ct)} + c.c. = \hat{\mathbf{q}}(x_2) e^{i\alpha[x_1 - (c_r + ic_i)t]} + c.c. \quad (10)$$

introduces the complex eigenvalue c , the real part of which may be interpreted as the phase speed, while the imaginary part is the amplification or the damping rate of the perturbation. (The complex conjugate is labelled $c.c.$)

A perturbation may initially be thought of as a linear superposition of monochromatic waves that develop in streamwise (and spanwise, if $\beta \neq 0$) periodic boxes of length $L_{x_1} = 2\pi/\alpha$ (and width $L_{x_3} = 2\pi/\beta$). Each wave travels on the base flow at its own constant phase speed c_r and grows or attenuates at its own rate $e^{\alpha c_i t}$. As time passes, just one of these waves dominates. This is the leading eigenmode and its calculation is the central part of instability analysis.

A complete instability analysis involves varying the Reynolds and wavenumber parameters and identifying the frequency and amplification/damping rate of the leading eigenmode. There are two particularly interesting curves in the (Re, α) plane. The first is the neutral curve, on which $\omega_i = 0$, which defines the boundary of stability/instability. The second is the maximum values of ω_i at fixed Re or fixed α . Both curves may be used to identify linear instability characteristics in experiments or simulations.

2.2 Spatial local stability

The assumption of a constant streamwise wavenumber may be relaxed and solutions of the LNSE may be sought for a constant real monochromatic frequency ω , treating α as the eigenvalue. From this point of view, linear perturbations are written as

$$\tilde{\mathbf{q}} = \hat{\mathbf{q}}(x_2) e^{i[(\alpha_r + i\alpha_i)x_1 + \beta x_3 - \omega t]} + c.c. \quad (11)$$

α_i being the (spatial) amplification or damping rate of the wave, while its wavenumber is α_r . This instability analysis framework is preferred by experimentalists because identification of perturbation characteristics is more straightforward when dealing with monochromatic waves. From a theoretical/numerical point of view, the eigenvalue problem to be solved is now nonlinear.

By integrating the spatial growth rate of convective perturbations, we can obtain *amplification* of their amplitude along the streamwise direction. This quantity is usually called the N – *factor* and is defined as

$$N = \ln \frac{A}{A_0} = - \int_{x_{1,0}}^{x_1} \alpha_i(x) dx, \quad (12)$$

where A is the amplitude of the perturbation and subscript $_0$ refers to the location where the perturbation first starts to grow. Smith & Gamberoni [15] and van Ingen [16] independently developed an empirical transition-prediction method using the N -factor values. The method assumes that transition occurs when relative amplification of discrete-frequency disturbances first reaches a preset ad hoc ‘transition level’ of $e^{N_{tr}}$. The critical value N_{tr} is found through correlation between computed N -factors and measured transition location. An extensive description of this method is given by Arnal [17]. Of course, transition location depends on the spectrum and the amplitude of perturbations present in the flow. Because the e^N method does not account for the initial amplitude of perturbations, the value of N_{tr} strongly depends on the perturbation environment. In order to get a reliable prediction of the transition location, the method should include a receptivity analysis, which provides the initial amplitude of the perturbation. Readers interested in the subject are referred to [18–24].

2.3 Phase velocity and group velocity

In expressions (5) and (6), setting $\beta = 0$ for convenience, the perturbations can also be written as $\tilde{\mathbf{q}}(\mathbf{x}, t) = \hat{\mathbf{q}}(x_2) \exp\{i\alpha(x_1 - ct)\}$ where $c \equiv \omega/\alpha$. For a given α , the value of $\tilde{\mathbf{q}}$ is therefore constant

Fig. 1. Waves often travel in packets and have a well-defined envelope. The phase velocity is the velocity at which the wave crests travel. The group velocity is the velocity at which the envelope travels.

along a particular ray with $(x_1 - ct) = \text{constant}$. For real α , c is therefore the velocity of the wave crests, which is the *phase* velocity. If (and only if) ω is directly proportional to α , then every wavenumber has the same phase velocity and the medium is known as *non-dispersive*.

In general, the perturbation consists of a superposition of many waves, which interfere with each other constructively and destructively. The patterns of constructive and destructive interference usually cause the perturbation to have an identifiable envelope, as shown in figure 1. If the wavecrests of all wavenumbers move at the same phase velocity, then this interference pattern, and therefore this envelope, also move at the phase velocity and they do not change shape over time. If, however, the wavecrests of different wavenumbers move at different phase velocities, then this interference pattern changes shape over time and the envelope moves at a different velocity to the wavecrests. The velocity of the envelope is known as the *group* velocity and it is equal to $d\omega/d\alpha$, as shown in [13, §191] In this case, the medium is known as *dispersive*.

2.4 Spatio-temporal stability

In a spatio-temporal stability analysis, both α and ω can be complex. It is then necessary to differentiate between three types of flow by considering the flow's response to an impulse. A flow is *stable* if the impulse response decays in every direction - i.e. along every ray emanating from the point of impulse. A flow is *convectively unstable* if the impulse response grows along some rays that move away from the point of impulse but decays at the point of impulse itself. A flow is *absolutely unstable* if the impulse response grows at the point of impulse. The review of Huerre & Monkewitz [25] is essential reading in this context and discusses several parallel flows to which this concept is applicable. Further details can be found in [26, 27]. The extension of this analysis to quasi-parallel flows led to one of the three contexts for the terminology *global instability*, which is used regularly in the literature. The theoretical bases of these contexts are distinct [12, 28].

2.5 The LNSE in 1D

After introduction of the modal ansatz (5) into (2) and (3), the LNSE become a generalized eigenvalue problem. For an incompressible flow, and with $(x_1, x_2, x_3) = (x, y, z)$, these are:

$$i\alpha\hat{u} + \hat{v}_y + i\beta\hat{w} = 0, \quad (13)$$

$$\mathcal{L}_{1d}\hat{u} - \bar{u}_y\hat{v} - i\alpha\hat{p} + i\omega\hat{u} = 0, \quad (14)$$

$$\mathcal{L}_{1d}\hat{v} - \hat{p}_y + i\omega\hat{v} = 0, \quad (15)$$

$$-\bar{w}_y\hat{v} + \mathcal{L}_{1d}\hat{w} - i\beta\hat{p} + i\omega\hat{w} = 0. \quad (16)$$

where $\mathcal{L}_{1d} \equiv \frac{1}{Re} \left[\frac{d^2}{dy^2} - (\alpha^2 + \beta^2) \right] - i\alpha\bar{u} - i\beta\bar{w}$, and the subscript y denotes d/dy . The analogous expansion and LNSE for compressible flows in which the local theory assumptions are satisfied may be found

in Mack [29]. Instability analysis based on (13-16) has been used extensively to describe instability of free-shear and boundary-layer flows. The key assumption made in the context of local theory is that of a *parallel-flow*, according to which the base flow velocity component \bar{v} , is *neglected*. Consequently, the basic state may comprise up to two velocity components, namely the streamwise $\bar{u}(y)$ and the spanwise $\bar{w}(y)$, both of which are functions of one spatial coordinate alone.

The boundary conditions completing the description of linear instability in the context of local theory are the viscous boundary conditions $\hat{u} = \hat{v} = \hat{w} = 0$ at solid walls or in the far-field (where the basic flow velocity vector assumes a constant value), alongside the boundary condition $\hat{v}_y = 0$, derived from the continuity equation. For flows that are unbounded in the normal direction, for example boundary-layer flows, the boundary conditions for perturbations can be relaxed and just require that \hat{u} , \hat{v} , \hat{w} is bounded as $y \rightarrow \infty$. This allows for solutions that propagate into or out from the boundary layer. For details see references [29, 30].

In compressible flow, use of the ansatz (5) and linearization leads to an analogous system for the determination of perturbation velocity components and disturbances to two of the three thermodynamic quantities: density, pressure and temperature. The system is closed with an appropriate equation of state, which can be that of ideal gases for the Mach number range $0 < Ma < 7$, before hypersonic flow sets in. Compressibility effects in linear stability will not be discussed here and the interested reader is referred to [29] and more recent reviews [31, 32].

2.6 The Orr-Sommerfeld equation

Returning to incompressible flow, the LNSE in 1D may be re-written in the form of a single ordinary differential equation, in which the disturbance pressure is eliminated. Eliminating the pressure perturbation by cross-differentiation of (14) and (16), using continuity (13), and substituting the result into (15), results in the Orr-Sommerfeld equation for the disturbance velocity component $\hat{v}(y)$,

$$\frac{i}{Re} \left[\hat{v}^{(4)} - 2k^2 \hat{v}'' + \alpha^4 \hat{v} \right] + (\alpha \bar{u} - \omega) \left[\hat{v}'' - k^2 \hat{v} \right] - \alpha \bar{u}'' \hat{v} = 0. \quad (17)$$

Primes denote differentiation with respect to y and $k = \sqrt{\alpha^2 + \beta^2}$. The boundary conditions $\hat{v} = \hat{v}' = 0$ at both ends of the integration domain complete the description of the problem.

As mentioned above, for open flows the boundary conditions $\hat{v} = \hat{v}' = 0$ may be replaced by \hat{v} , \hat{v}' being bounded as $y \rightarrow \infty$. In the case of constant basic state far from the wall, $\bar{u} = U_\infty$, equation (17) has asymptotic solutions $\hat{v}_n = \exp(\lambda_n y)$ with $\lambda_{1,2} = \pm \sqrt{i\alpha Re(U_\infty - c) + k^2}$ and $\lambda_{3,4} = \pm k$. For a choice of parameters that makes λ_n pure imaginary, the solutions \hat{v}_n yield inwards/outwards propagating waves in the y direction with constant amplitude.

By using Squire's transformation, $\alpha_{2d} = k$ and $\alpha_{2d} Re_{2d} = \alpha Re$, one can show that, to each three-dimensional Orr-Sommerfeld mode there corresponds a two-dimensional one at a lower Reynolds number. This yields that two-dimensional flows first become unstable to modes with $\beta = 0$.

2.7 The Rayleigh equation

The instability of base flows having inflectional profiles, e.g. the shear layer, may be analysed by solution of the Rayleigh equation

$$(\alpha \bar{u} - \omega) \left[\hat{v}'' - \alpha^2 \hat{v} \right] - \alpha \bar{u}'' \hat{v} = 0, \quad (18)$$

which may be obtained from the Orr-Sommerfeld equation in the limit $Re \rightarrow \infty$. The no-penetration boundary condition $\hat{v} = 0$ completes the description of the instability problem. From a physical point

```
../figures/model_2.pdf
```

Fig. 2. The base flows in this tutorial are all planar jets/wakes with top hat velocity profiles. These flows have analytical dispersion relations, which can be calculated without numerical methods.

of view, the implicit assumption in this class of analysis is that viscosity does not affect stability. The vanishing of viscosity has the potential to introduce singularities that need to be circumvented in the numerical solution.

2.8 Tutorial on local stability analysis

A simple class of flows can give useful insight into the instability mechanisms active in more realistic flows. These base flows, which have piecewise linear or top hat velocity profiles, support perturbations with analytical relationships between ω and α . These analytical expressions replace the numerical solutions to the LNSE (13–16), Orr-Sommerfeld (17), and Rayleigh equations (18), which were for flows with smooth velocity profiles. This Matlab tutorial provides an introduction to temporal, spatial, and spatio-temporal stability analysis as applied to these base flows. For base flows with real velocity profiles, these techniques need to be combined with the numerical solution methods described in sections 2.9 and 6. In this tutorial, the streamwise wavenumber, α , is given the symbol k , which is the notation in much of the literature.

2.8.1 The dispersion relations for simple flows

Most analyses of local stability are performed by solving the O–S equation numerically using spectral methods in one dimension. Before such methods were available, dispersion relations for a few simple flows were derived analytically. These dispersion relations are used in this section because their qualitative behaviour is much the same as that of the O–S equation, but they are easier to derive, understand, manipulate, and analyse. They have come from [13] §§365 – 369, [14] §§4–5, [33] and [34]. They are expressed in dimensionless form in the format preferred by [27]: as a function that equals zero: $D \equiv f(\omega, k) = 0$. It is easiest to explain the flow with the most features first and then simplify it by removing the features one by one.

The flow with the most features is shown in figure 2. It is a planar flow consisting of a central flow with density ρ_1 , velocity U_1 and width $2h_1$, surrounded by two flows with density ρ_2 , velocity U_2 and width h_2 . The velocities and densities are uniform except at the shear layers between the fluids, where they jump discontinuously across an interface that has surface tension σ . We will consider only varicose

perturbations, in which the shear layers move in opposite directions, and sinuous perturbations, in which the shear layers move in the same direction. Any perturbation can be expressed as a linear combination of a varicose and sinuous perturbation. The dimensionless parameters are

- the shear ratio $\Lambda \equiv (U_1 - U_2)/(U_1 + U_2)$;
- the density ratio $S \equiv \rho_1/\rho_2$;
- the confinement ratio h_2/h_1 ;
- the surface tension $\Sigma \equiv 4\sigma/(h_1\rho_2(U_1 + U_2)^2)$.

Various symmetries in the model become more apparent if a slightly different set of reference scales and dimensionless parameters are used [35], but the dispersion relations become less easy to read.

The dispersion relations are

varicose perturbations of a confined planar jet/wake

$$D \equiv S(1 + \Lambda - \omega/k)^2 \coth(\xi) + (1 - \Lambda - \omega/k)^2 \coth(\xi h) - \xi \Sigma = 0 \quad (19)$$

sinuous perturbations of a confined planar jet/wake

$$D \equiv S(1 + \Lambda - \omega/k)^2 \tanh(\xi) + (1 - \Lambda - \omega/k)^2 \coth(\xi h) - \xi \Sigma = 0 \quad (20)$$

varicose perturbations of an unconfined planar jet/wake

$$D \equiv S(1 + \Lambda - \omega/k)^2 \coth(\xi) + (1 - \Lambda - \omega/k)^2 - \xi \Sigma = 0 \quad (21)$$

sinuous perturbations of an unconfined planar jet/wake

$$D \equiv S(1 + \Lambda - \omega/k)^2 \tanh(\xi) + (1 - \Lambda - \omega/k)^2 - \xi \Sigma = 0 \quad (22)$$

perturbations of an unconfined single shear layer

$$D \equiv S(1 + \Lambda - \omega/k)^2 + (1 - \Lambda - \omega/k)^2 - \xi = 0 \quad (23)$$

($\Sigma = 1$ for an unconfined single shear layer because the surface tension defines the reference length-scale h_1)

The variable ξ is required in order to keep branch points off the k_r axis, as described in [36] and [34]. It is given by $\xi \equiv +(k^2 + k_y^2)^{1/2}$ as $k_y \rightarrow 0$. Here, however, we shall examine only $k \geq 0$ and therefore ξ can be replaced by k .

Surface tension is required in order to prevent ω from becoming infinite as k becomes infinite. Surface tension has a strong effect on absolute instability, however, as described in [35]. An alternative strategy is to introduce a finite shear layer thickness. This prevents ω from becoming infinite and has only a mild effect on long wavelength instabilities. Analytical dispersion relations exist for the analogous flows [34].

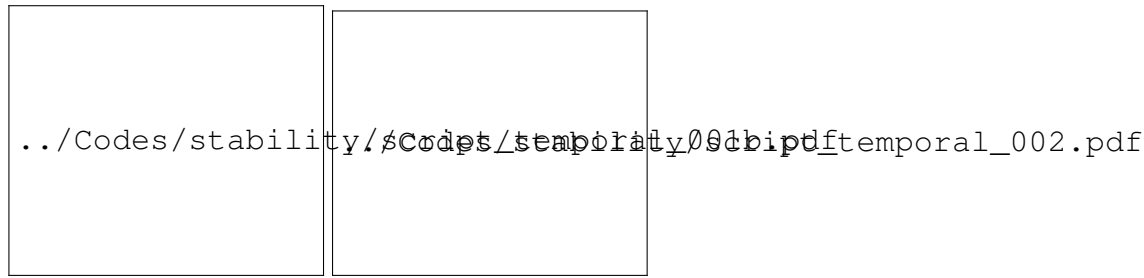


Fig. 3. Left: the imaginary and real components of $\omega(k)$ calculated with a temporal stability analysis, in which k is constrained to be real. Right: the imaginary components of $\omega(k)$ for the five dispersion relations.

2.8.2 Coding the dispersion relations

It is quite easy (but rather tedious) to use the quadratic formula to derive $c \equiv \omega/k$ as an analytic function of k . It is quicker to use Matlab functions. The function `fun_eval_c_single.m` uses the quadratic formula to evaluate the two values of c for a given value of k . (In order to produce smooth plots, it also swaps Matlab's default ordering of the two solutions at certain values of k . This does not become important until we consider the spatio-temporal analysis in section 2.8.7.)

The function has been constructed so that entire arrays of `c1` and `c2` can be calculated simultaneously. This requires operators such as `(.*)` to be used instead of `(*)`. The parameters Λ and S are held in a Matlab structure as `param.L` and `param.S`. This notation makes it easy for a single script to call a variety of functions.

1. Write Matlab functions to calculate ω/k for the remaining dispersion relations. Name them

```
fun_eval_c_unconf_jetwake_sin.m
fun_eval_c_unconf_jetwake_var.m
fun_eval_c_conf_jetwake_sin.m
fun_eval_c_conf_jetwake_var.m
```

2. Try calling these functions with the generic functions `fun_eval_c.m` and `fun_eval_w.m` in order to become familiar with the program structure.
3. With the exception of the single shear layer, iterative procedures are required in order to find k as a function of ω . These involve setting the function D to zero by changing k at given ω . Write Matlab functions to calculate D for each dispersion relation, given ω and k . Name them

```
fun_eval_D_single.m
fun_eval_D_unconf_jetwake_sin.m
fun_eval_D_unconf_jetwake_var.m
fun_eval_D_conf_jetwake_sin.m
fun_eval_D_conf_jetwake_var.m
```

4. Try calling these functions with the generic function `fun_eval_D.m`.
5. Write a script that calculates ω using the first set of functions and then checks that this (ω, k) pair satisfies $D = 0$ by calling the second set of functions.

These functions will be the building blocks for the rest of this tutorial.

2.8.3 Temporal stability analysis

In a temporal stability analysis, we constrain k to be a real number. Physically, this means that we consider only waves that do not grow or decay in the streamwise direction. We then ask whether such

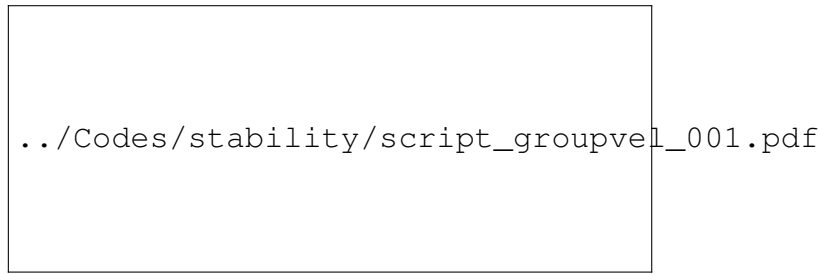


Fig. 4. The phase velocity (solid lines) and group velocity (dashed lines) as a function of wavenumber, k , for a single shear layer with surface tension. This is a dispersive medium, which means that waves at different wavenumbers travel at different speeds and that the group velocity does not, in general, equal the phase velocity.

waves grow or decay in time. An example is shown in figure 3 (left) for a single shear layer with $\Lambda = 0.9$ and $S = 1$.

1. Write a script called `script_temporal_001.m` to generate figure 3 (left).
2. There are two regimes, either side of $k = 1.6$. How do the waves behave in these two regimes?
3. Vary Λ and S to see how this model behaves.
4. Write a script called `script_temporal_002.m` to perform the temporal analysis on all the dispersion relations and to plot their growth rates as a function of positive k on the same plot, as shown in figure 3(right).
5. What do you observe? In particular, how does confinement affect the temporal stability of the flows?

2.8.4 Group velocity

The phase velocity $c \equiv \omega/k$ is the velocity of wavecrests. The group velocity $c_g \equiv d\omega/dk$ is the velocity of wavepackets. In a dispersive medium, $c \neq c_g$.

1. Write a function called `fun_eval_dwdk.m` to evaluate the group velocity as a function of k . A first order finite difference method will be good enough.
2. Write a script called `script_groupvel_001.m` to compare the phase and group velocities as shown in figure 4.
3. Investigate the different dispersion relations at different parameter values. What do you observe? Look particularly at unconfined low density jets ($\Lambda \sim 1, S \ll 1$) at small values of Σ .

2.8.5 Spatial stability analysis

In a spatial stability analysis, we constrain ω to be a real number. Physically, this means that we force sinusoidally at a particular point in space and see whether the resulting perturbations grow (negative k_i) or decay (positive k_i) in space. This is known as the *signalling problem*.

Algorithm `fun_eval_k.m` uses an iterative technique to find k , given ω and an initial guess for k . It uses Matlab's function `fsolve.m`, which tries to set the output, `D`, of `fun_eval_D_loc` to zero by varying its argument k . This is where the functions `fun_eval_D_*.m` become useful.

1. Write a script called `script_spatial_001.m` to perform a spatial stability analysis on a single shear layer with $\Lambda = 0.5$ and $S = 1$, as shown in figure 5.
2. At small ω , the iterative procedure finds a second solution. Try changing the initial guess for k so that it always finds the first solution.
3. What is the most amplified frequency?
4. What happens to the most amplified frequency as Λ increases?



Fig. 5. The real and imaginary components of k , calculated with a spatial stability analysis, in which ω is constrained to be real. Left: the exact spatial analysis, performed via iteration from a guessed value of k . Right: the approximate spatial analysis from Gaster's transformation, compared with the exact spatial analysis.

Spatial stability analyses are more difficult to perform than temporal stability analyses and, as we shall see later, have no physical relevance when the flow is absolutely unstable because the transient behaviour overwhelms the signal if the wave with zero group velocity has positive growth rate.

2.8.6 Gaster's transformation

The relationship between temporal and spatial stability is given in [37]. The angular frequency and wavenumber pairs from the temporal analysis are labelled $\omega(T)$ and $k(T)$ respectively. The angular frequency and wavenumber pairs from the spatial analysis are labelled $\omega(S)$ and $k(S)$ respectively. These are approximately related by:

$$k_r(S) \approx k_r(T), \quad (24)$$

$$\omega_r(S) \approx \omega_r(T), \quad (25)$$

$$\frac{\omega_i(T)}{k_i(S)} \approx -\frac{\partial \omega_r}{\partial k_r}. \quad (26)$$

The final term in (26) can be written $-\text{Re}(d\omega/dk)$ and is simply the real component of the group velocity.

1. Write a script called `script_spatial_002.m` to compare $k_i(\omega_r)$ calculated with `script_spatial_002.m` with that calculated from Gaster's transformation, as shown in figure 5 (right). (You can use Gaster's transformation to improve the initial guess of k for the spatial analysis.)
2. Vary S and Λ to discover when Gaster's transformation works well and when it works badly.

Gaster's transformation begs the question of what happens when the real part of the group velocity is zero. Is the spatial growth rate infinite? Rather than ponder this conundrum now, it is better to progress to a spatio-temporal stability analysis, which will make everything clear.

```
../Codes/stability/script_spatemp_001.pdf
```

Fig. 6. Contours of $\omega_i(k)$ (greyscale) and $\omega_r(k)$ (grey lines) for a single shear layer with $\Lambda = 0.9$, $S = 1$. This is a spatio-temporal stability analysis in which both ω and k are complex. The points with $d\omega/dk = 0$ can be identified by eye (there is one in each frame). The thick black line is $\omega_i = 0$.

2.8.7 Spatio-temporal stability analysis

In a spatio-temporal analysis, k and ω are both allowed to be complex numbers. Physically, this means that we consider waves that grow or decay in the streamwise direction and that grow or decay in time. A useful way to picture this is to imagine exciting every wave simultaneously with an impulse at $(x, t) = (0, 0)$ and then observing the evolution of the resulting wavepacket. This is known as an *impulse response* or, equivalently, the *Green's function*. The response to any type of forcing can be found from this by convoluting the impulse response with the forcing signal.

Only some waves are permitted (these are the ones that satisfy the dispersion relation). They propagate away from the point of impulse at different velocities, given by their *group velocity* $d\omega/dk$, and grow or decay at different rates, given by their growth rate, ω_i .

If every wave decays in time then the flow is *stable*. If some waves grow in time then the flow is *unstable* and a further distinction is necessary. After a long time, the only wave to remain at the point of impulse is the wave that has zero group velocity. If this wave decays in time, then the impulse response decays to zero at the point of impulse and the flow is called *convectively unstable*. If the wave grows in time, then the impulse response grows to infinity at the point of impulse and the flow is called *absolutely unstable*.

In the next section, we will examine this in more detail. For now, however, we will find the wave with zero group velocity by plotting contours of ω in the complex k -plane.

1. For the single shear layer, write a script called `script_spatemp_001.m` to calculate ω_1 and ω_2 on a grid of complex k with $k_r \in [0, 2]$ and $k_i \in [-1, 1]$. Plot contours of ω_i and ω_r on the same plot, as in figure 6. (The `stencil` becomes useful here.) Plot the contour $\omega_i = 0$ with double thickness.
2. What do you notice about the relationship between the contours of ω_i and the contours of ω_r ?
3. Identify by eye the position where the group velocity is zero. Does it have positive or negative growth rate?
4. Write a function called `fun_eval_dwkd0.m` that uses `fsolve` to converge to this point, given an initial guess, and then displays (ω, k) at this point.
5. Write a script called `script_click.m` that asks the user to click near a point where $d\omega/dk = 0$,

../figures/Fig_034_v1.pdf

Fig. 7. The impulse response for varicose perturbations of an unconfined low density jet with $\Lambda = 1/1.1$, $S = 0.1$, and finite thickness shear layers. The impulse is at $(x, z) = (0, 0)$ and the resultant waves disperse at their individual group velocities in the x and z directions. The chart plots the growth rate, ω_i , of the wave that dominates along each ray $(x/t, z/t)$, *i.e.* the wave that has group velocity $(x/t, z/t)$. We see that most of the wavepacket propagates and grows downstream (to the right) but that some waves propagate and grow upstream (to the left). The growth rate at the point of impulse $(x/t, z/t) = (0, 0)$ is positive, which means that this is an absolutely unstable flow.

then converges accurately to that point, then determines whether the flow is absolutely or convectively unstable.

The contours of ω_i and ω_r are always at right angles to each other. Furthermore, the two components of curvature on the surface $\omega_i(k)$ always have opposite sign. This means that points where $d\omega/dk = 0$ are *saddle points* of $\omega(k)$. In the long time limit, the impulse response at the point of impulse is dominated by the behaviour of these saddle points. At a saddle point, the values of ω and k are called the *absolute* frequency and wavenumber and are given the symbols ω_0 and k_0 .

1. Compare figure 3 with figure 6 to check that the temporal analysis corresponds to a slice through $\omega(k)$ along the k_r axis.
2. What does the spatial analysis correspond to in figure 6?
3. Explain why a spatial analysis does not work for absolutely unstable flows.

2.8.8 The Briggs-Bers criterion

The aim of this section is to present a more rigorous calculation of the impulse response and to show that some saddle points do not contribute to it. We want to evaluate

$$\mathbf{u}(x, t) = \int_{-\infty}^{\infty} \int_{-\infty}^{\infty} \hat{\mathbf{u}}(k, \omega) e^{i(kx - \omega t)} d\omega dk. \quad (27)$$

To evaluate the response at the point of impulse, see [38], particularly equation (9), and [27], which gives more steps in the calculation. To evaluate the response at every point in space, see [36], particularly figure 11, and [34], one result from which is shown in figure 7.

Figure 7 shows contours of the growth rate as a function of group velocity, $(x/t, z/t)$, for all the permitted waves in the impulse response. (It is for varicose perturbations of an unconfined low density jet with $\Lambda = 1/1.1$ and $S = 0.1$.) The impulse response propagates and grows at the point of impulse, $(x/t, z/t) = 0$, so this flow is absolutely unstable. It grows fastest, however, in the downstream direction, $x/t > 0$. The maximum growth rate of the impulse response (8.5) is given by the growth rate of the temporal stability analysis because, at this point in the impulse response, $k_i = 0$.

The integral (27) can be evaluated by integrating either over ω and then k , or over k and then ω . For these dispersion relations, it easiest to integrate over ω first because, for each k , there are only two permitted



Fig. 8. Contours of $\omega_i(k)$ for varicose perturbations of a confined jet flow with surface tension, showing the integration path from $k = -\infty$ to $k = +\infty$. The integration path passes over saddle points S_1 and S_3 , which means that they contribute to the integral. It does not pass over saddle points S_{2a} or S_{2b} , however, which means that they do not contribute to the integral. This is another way to visualize the Briggs-Bers criterion, which states that a saddle point is only valid if it is pinched between a k^+ and a k^- hill.

values of ω . The integral becomes

$$\mathbf{u}(x, t) = \int_{-\infty}^{\infty} \hat{\mathbf{u}}(k, \omega) e^{i(kx - \omega_1(k)t)} dk + \int_{-\infty}^{\infty} \hat{\mathbf{u}}(k, \omega) e^{i(kx - \omega_2(k)t)} dk. \quad (28)$$

Initially, the integration path lies on the real k -axis but it can be shifted into the complex k -plane without changing the integral, as long as it is not shifted through branch points or poles (*i.e.* points where $\omega = \pm\infty$). The integral is easiest to evaluate if the integration path is shifted onto lines of constant ω_r because then the phase of $\exp\{i(kx - \omega t)\}$ remains constant and the integrand does not oscillate as k changes. (Remember that $x = 0$ because we are looking at the point of impulse, so the only term that can oscillate as k varies is $\exp(i\omega_r(k)t)$.)

In order to pass from $k = -\infty$ to $k = +\infty$, the integration path must cross some (but not all) of the saddle points in the k -plane and, for each of these saddle points, there is only one possible value of ω_r . This

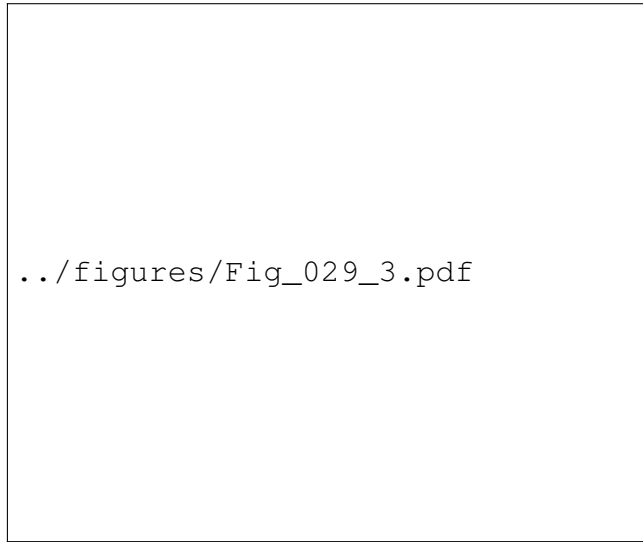


Fig. 9. Contours of $\omega_i(k)$ for the same flow as figure 8, as the surface tension is reduced. This reduction in Σ causes the s_1 saddle to move to lower ω_i and therefore causes the integration path to pass over the s_{2a} saddle point. When the surface tension tends to zero (not shown here) all the s_2 saddle points move onto the integration path.

means that the integration path must cross these saddle points at this value of ω_r and then change to another value of ω_r at points where ω_i is strongly negative, so that the oscillating contribution to the integral there is negligible.

This is best explained by showing an example. Figure 8 shows contours of $\omega_i(k)$ for varicose perturbations of a confined jet flow with $\Lambda = 1$, $S = 1$, $h = 1.3$, $\Sigma = 1$. The integration path needs to pass over two saddle points, s_1 and s_3 , in order to pass from $k = 0$ to $k = \infty$, but it misses out saddles s_{2a} and s_{2b} . As the surface tension reduces, which is shown in figure 9, saddle s_{2a} comes onto the integration contour. As it reduces further, s_{2b} etc. come onto the contour too.

In the long time limit, the dominant contribution to the integral comes from the point on the integration path with highest ω_i , which is always a saddle point. At these saddle points, contours of constant ω_r extend into the top half k -plane on one side and into the bottom half k -plane on the other side. This is the Briggs-Bers criterion. It is another way of stating that the saddle point must lie on the integration path. Alternative but equivalent explanations can be found in [?, 38].

1. Write a script called `script_spatemp_002.m` to plot $\omega_1(k)$ for varicose perturbations of a confined jet/wake flow with $\Lambda = 1$, $S = 1$, $h = 1.3$, $\Sigma = 1$. Compare it with figure 9.
2. Investigate how the dominant saddle points change as S decreases, Σ decreases, and h increases. Look particularly at the s_{2a} saddle.
3. Write a script called `script_spatemp_003.m` to repeat this for varicose perturbations of an unconfined jet/wake flow with $\Lambda = 1$, $S = 1$, $\Sigma = 0$. This corresponds to an unconfined jet. Find the s_{2a} saddle point exactly with `script_click.m`

The main point of this section is that only some saddle points contribute to the impulse response and that, in the case of a low density jet with vanishing surface tension, the s_{2a} saddle is one of these.



Fig. 10. Eigenvalue spectrum for plane Poiseuille flow (PPF) at $Re = 10^4$, $\alpha = 1$, $\beta = 0$. Solution of LNS (●) and Orr-Sommerfeld (□) equations. Notice that the vorticity modes are not represented by Orr-Sommerfeld equation. Results produced by `run_LNS.m` and `run_OS.m`.

2.9 Application to wall-bounded shear-flow: plane Poiseuille flow

One of the most studied two-dimensional flows is the flow between two parallel walls (Plane Poiseuille flow - PPF). This flow, which is invariant in the streamwise direction, can be described as

$$\bar{\mathbf{u}} = (U(y), 0, 0), \quad U(y) = 1 - y^2, \quad y \in [-1, 1]. \quad (29)$$

Plane Poiseuille flow, the instability of which was first solved by spectral methods in the classic paper of Orszag [39], serves as the testbed for implementation and validation of a stability analysis on a realistic flow.

This section presents results that may be obtained with the code provided for the Tutorial work. The stability problem is solved either in its original generalized form (13-16) or considering the Orr-Sommerfeld equation (17). To solve the stability equations, we discretize the equations using the spectral collocation method using Chebychev polynomials, as shown in the Appendix. This yields a generalized matrix eigenvalue problem of the form

$$\mathbf{A}\hat{\mathbf{q}} = \omega\mathbf{B}\hat{\mathbf{q}}, \quad (30)$$

where $\hat{\mathbf{q}} = (\hat{u}, \hat{v}, \hat{w}, \hat{p})^T$ for discretized equations (13-16) or $\hat{\mathbf{q}} = \hat{v}$ for the Orr-Sommerfeld equation. In figure 10, the spectrum of the eigenvalues for $Re = 10^4$, $\alpha = 1$ and $\beta = 0$ is plotted. Figure 11 presents the velocity and pressure perturbations corresponding to the most unstable eigenvalue.


The following tutorial exercises are recommended:

1. Familiarize yourself with the codes provided. Script `run_LNS.m` computes the eigenvalue and eigenfunctions corresponding to equations (13-16) and script `run_OS.m` to equation (17).
2. Run the scripts for $Re = 10^4$, $\alpha = 1$ and $\beta = 0$ by changing the values of parameters `Re`, `alpha` and `beta` in file `run_OS.m` (and `run_LNS.m`).
3. Change the number of Chebychev polynomials and investigate convergence of the most unstable mode (the one with the largest ω_i) as well as the whole spectrum. Compare your results with those of Kirchner [40] $\omega = 0.2375264888204682 + 0.0037396706229799i$.



```
./Figures/PPF_eigvec.pdf
```

Fig. 11. Velocity and pressure perturbations corresponding to the most unstable eigenvalue of plane Poiseuille flow (PPF) at $Re = 10^4$, $\alpha = 1$, $\beta = 0$. Data produced by `run_LNS.m` for the most unstable mode in figure 10. All components are normalized with $\max(|\hat{u}|)$.



```
./Figures/Michalke.pdf
```

Fig. 12. Growth rate as a function of wave number for the `tanh` profile. Data from Michalke [41]

4. Compare the results of the two scripts `run_LNS.m` and `run_OS.m`.
5. Plot the eigenfunctions of different modes to see the characteristic shape of different branches of the spectrum.

2.10 Free shear-flow: the `tanh` profile

Chebyshev Gauss–Lobatto-spaced points are not always conveniently-spaced. In this tutorial, the Rayleigh equation is solved for perturbations to a `tanh` velocity profile, which has high gradients around $y = 0$ and has infinite extent in the y -direction. In order to solve this, a mapping function needs to be introduced. The following tutorial exercises are recommended:

1. Familiarize yourselves with the codes provided.
2. Change the base flow and its derivatives in script `run_OS.m` to those for the hyperbolic tangent

profile

$$\bar{u}(y) = \tanh(y). \quad (31)$$

3. Implement the following mapping

$$y = -l \hat{y} / \sqrt{(1 + s - \hat{y}^2)}. \quad (32)$$

where $l = 10$, $s_\infty = 20$, $s = (l/s_\infty)^2$, into the differentiation matrices, along the lines presented in equations (75-78).

4. Modify the function `OS_temp.m` to solve the Rayleigh equation.
5. Run the code for parameters in the classic work of Michalke [41] and compare the results. The data form Michalke is stored in file `Michalke.dat` and plotted in figure 12. Note that the real part of phase velocity for this flow is independent of wavenumber α and is equal to 1.
6. Compare results for the Orr-Sommerfeldt and Rayleigh equations.

3 Secondary linear modal instability theory

The linear instability of wall-bounded shear flows has been studied for over a century. The latter stage of the linear instability process in a boundary layer is of particular interest, motivated by the turbulent breakdown of laminar linearly unstable flow. The key point is to discover the scenario that follows linear amplification of small-amplitude perturbations in a boundary layer. However small such perturbations may be initially, the exponential nature of modal growth suggests that these perturbations must reach amplitudes at which the linearity assumption is invalidated. There exists a theoretical vacuum between the arbitrarily-scalable results of linear local theory and the essentially nonlinear nature of the phenomenon of transition to turbulence.

A breakthrough was provided by the almost simultaneous independent theoretical [42–44], experimental [45,46] and DNS [47,48] efforts in the area of secondary (linear modal) instability theory. The analysis proceeds by considering a steady laminar one-dimensional basic flow, $\bar{\mathbf{q}}$, which has been modified by the linear growth of its most unstable perturbation, $\hat{\mathbf{q}}$. In order for the secondary instability analysis to remain linear, the amplitude, A , at which the (so-called primary) eigenmode needs to be superposed upon the basic state needs to be small initially, but is subsequently allowed to become finite and modify the steady laminar basic state in a periodic manner, while linear theory is still valid. In a temporal framework the ensuing new two-dimensional basic state

$$\begin{aligned} \bar{\mathbf{q}}_{2d}(x, y, t) &= \bar{\mathbf{q}}_{2d}(x + 2\pi/\alpha, y, t) = \\ \bar{\mathbf{q}}(y) &+ A \left(\hat{\mathbf{q}}(y) e^{i[\alpha x - (\omega_r + i\omega_i)t]} + c.c. \right) \end{aligned} \quad (33)$$

is periodic in a frame of reference moving with the phase speed of the leading eigenmode (the Tollmien-Schlichting - TS wave) with a periodicity length $L_x = 2\pi/\alpha$, where α is the wavenumber of the most amplified TS mode. Consequently, Floquet theory is used to analyze the modified base state, three-dimensional perturbations assuming the form [44]

$$\tilde{\mathbf{q}}(x, y, t) = e^{\sigma t} e^{\gamma x} e^{i\beta z} \hat{\mathbf{q}}(x, y). \quad (34)$$



Fig. 13. Subharmonic secondary growth rate σ as a function of the spanwise wave number β for $F = 10^6 \alpha c_r / Re = 124$ at Branch II, $Re = 606$ [44]. The parameter A indicates the amplitude of the primary disturbance as a percentage of the maximum value of the streamwise basic flow velocity component.

Two interesting classes of linear secondary perturbations have been identified in experiments [45, 49] and are modeled in secondary linear theory, *fundamental* perturbations, for which

$$\hat{\mathbf{q}}_f(x, y) = \sum_{m \text{ even}} q'_f(y) e^{im \frac{\alpha}{2} x}, \quad (35)$$

and *subharmonic*, for which

$$\hat{\mathbf{q}}_s(x, y) = \sum_{m \text{ odd}} q'_f(y) e^{im \frac{\alpha}{2} x}, \quad (36)$$

respectively satisfying

$$\hat{\mathbf{q}}_f(x, y, t) = \hat{\mathbf{q}}_f(x + L_x, y, t) \quad (37)$$

and

$$\hat{\mathbf{q}}_s(x, y) = \hat{\mathbf{q}}_s(x + 2L_x, y). \quad (38)$$

The ansatz (33) alongside either of (35) or (36) is introduced into the LNSE, like-order terms are grouped together and an eigenvalue problem is obtained for the determination of the secondary growth rate σ as a function of the flow parameters, Re , the streamwise and spanwise wavenumbers, α and β , respectively, given an (arbitrarily chosen) amplitude parameter A ; figure 13 shows results for subharmonic resonance in the Blasius boundary layer.

From a physical point of view, secondary instabilities represent lambda vortices formed during the late stages of transition. Fundamental instabilities, also known as K-type instabilities, are aligned with each

other, while subharmonic instabilities, also known as H-type instabilities, form a staggered pattern of vortices. Both are clearly visible in experiments on both flat plate and axisymmetric boundary layers. Excellent agreement is obtained between theoretical results of secondary instability theory and DNS in the plane Poiseuille flow [47, 50]. In the celebrated experiments of Kachanov and Levchenko [45, 46] both three-dimensional spatial distribution of lambda vortices as well as secondary amplification rates σ were measured during transition in the Blasius boundary layer and the result were found to be in excellent agreement with the predictions of the subharmonic H-type scenario. Although the amplitude parameter A in (33) can be chosen to match experimentally-measured amplitudes of the primary instability, an alternative approach which altogether abandons the modal concept for the description of boundary layer stability, namely the Parabolized Stability Equations (PSE) [11], has overshadowed secondary stability theory, on account of the potential of PSE to predict both linear and nonlinear disturbance growth in a self-consistent manner. The PSE is discussed next.

4 Non-local nonparallel theory - the PSE

Traditional stability theory, based on the quasi-parallel flow assumption, does not account for growth of the boundary layer. The *local* character of this theory exclude any history effects associated with the initial condition or the varying properties of the basic flow. Early work on the effects of a growing boundary layer on the characteristics of the disturbances was based on the multiple-scales method (Bouthier [51], Gaster [52], Saric & Nayfeh [53], Gaponov [54] and El-Hady [55]). Recent work by Zuccher & Luchini [24] gives a good review of the application of the multiple-scales method for receptivity analysis.

The idea of solving parabolic evolution equations for disturbances in the boundary layer was first introduced by Hall [56] for steady Görtler vortices. Itoh [57] derived a parabolic equation for small-amplitude Tollmien-Schlichting waves. Herber & Bertolotti [58], and Bertolotti, Herbert & Spalart [59] developed this method further and derived the non-linear parabolized stability equations (PSE). Simen & Dallmann [60] independently developed a similar theory. Their contribution was to consistently and in a general way model convectively amplified waves with divergent and/or curved wave-rays and wave-fronts propagating in non-uniform flow. Due to the fact that the disturbance characteristics predicted by such a method are influenced by local and upstream flow conditions, this theory is called *non-local*.

It should be mentioned that the parabolic stability equations constitute an initial value problem and in principle can be used to compute the evolution of any perturbation. However, the auxiliary conditions (see section 4.2) usually cause the solution to converge to the most unstable (or least stable) mode. Starting the integration with the dominant mode given by local theory, it always converges to the non-local solution for that mode. The linearised boundary-layer equations, which are similar to PSE but with $\alpha = 0$, have been used by Andersson, Berggren and Henningson [61], and Luchini [62] to compute the optimal transient growth in Blasius boundary layer. Recently, Tempelmann, Hanifi and Henningson [63, 64] modified PSE to compute the optimal perturbation in three-dimensional boundary layers. Next we discuss the basics of the non-local method. A detailed discussion on this subject can be found in Bertolotti [65] and Herbert [66].

4.1 Assumptions

Here, we restrict ourselves to quasi-three dimensional flows (basic flows which are independent of the z coordinate). We start the derivation of the non-local stability equations by introducing the following assumptions:

1. The first assumption is of WKB type, in which the dependent variables are divided into an amplitude function and an oscillating part, i.e.

$$\tilde{\mathbf{q}}(\mathbf{x}, t) = \hat{\mathbf{q}}(x, y) \exp \left\{ i \left[\int_{x_0}^x \alpha(x') dx' + \beta z - \omega t \right] \right\}, \quad (39)$$

Here, as in the spatial local theory, α is a complex number. Note that in non-local theory, in contrast to the local theory, both the shape function, $\hat{\mathbf{q}}$, and the phase function, Θ , are allowed to vary in the streamwise direction.

2. As a second assumption, a scale separation $1/Re$ is introduced between the weak variation in the x -direction and the strong variation in the y -direction, analogous to the multiple-scales method. Important implications of this assumption are that the x -dependence of the basic and disturbance flow, and the normal basic flow velocity component V are also assumed to scale with the small parameter $1/Re$.

$$\frac{\partial}{\partial x}, V \approx O(Re^{-1}), \quad \frac{\partial}{\partial y}, U, W \approx O(1). \quad (40)$$

With the above scaling and ansatz (39) introduced into the linearized Navier–Stokes equations, considering only terms that scale with powers of Reynolds number up to $1/Re$, we obtain the non-local, linear stability equations which are *nearly* parabolic. They describe the kinematics, nonuniform propagation and amplification of wave-type disturbances with divergent or curved wave rays in a nonuniform basic flow. These equations can be written as

$$\mathcal{A}\hat{\mathbf{q}} + \mathcal{B}\frac{\partial\hat{\mathbf{q}}}{\partial y} + \mathcal{C}\frac{\partial^2\hat{\mathbf{q}}}{\partial y^2} + \mathcal{D}\frac{\partial\hat{\mathbf{q}}}{\partial x} = 0. \quad (41)$$

The entries of these matrices for an incompressible boundary layer are

$$\mathcal{A} = \begin{bmatrix} i\alpha & 0 & i\beta & 0 \\ \zeta + \frac{\partial U}{\partial x} & \frac{\partial U}{\partial y} & 0 & i\alpha \\ 0 & \zeta + \frac{\partial V}{\partial y} & 0 & 0 \\ \frac{\partial W}{\partial x} & \frac{\partial W}{\partial y} & \zeta & i\beta \end{bmatrix}, \quad \mathcal{B} = \begin{bmatrix} 0 & 1 & 0 & 0 \\ V & 0 & 0 & 0 \\ 0 & V & 0 & 1 \\ 0 & 0 & V & 0 \end{bmatrix},$$

$$\mathcal{C} = \begin{bmatrix} 0 & 0 & 0 & 0 \\ -\frac{1}{Re} & 0 & 0 & 0 \\ 0 & -\frac{1}{Re} & 0 & 0 \\ 0 & 0 & -\frac{1}{Re} & 0 \end{bmatrix}, \quad \mathcal{D} = \begin{bmatrix} 1 & 0 & 0 & 0 \\ U & 0 & 0 & 1 \\ 0 & U & 0 & 0 \\ 0 & 0 & U & 0 \end{bmatrix},$$

where

$$\zeta = -i\omega + i\alpha U + i\beta W + \frac{1}{Re}(\alpha^2 + \beta^2).$$

The corresponding terms for compressible flows given in a curvilinear coordinate system can be found in Ref. [67, 68].

The disturbances are subjected to the following boundary conditions

$$\hat{u} = 0 \text{ on } y = 0 \text{ and } \hat{u} \rightarrow 0 \text{ as } y \rightarrow \infty. \quad (42)$$

where \hat{u} is the perturbation velocity. The system of equations (41) is integrated in the downstream direction with the initial condition given by the solution of the local stability theory at $x = x_0$.

4.2 Auxiliary condition

As both the amplitude and phase function depend on the x -direction, we follow [65], [69] and [66] and remove this ambiguity by specifying various forms of ‘auxiliary’ conditions. These conditions can be based either on the amplitude of one of the disturbance quantities \hat{q}_k of equation (41) at some fixed $y = y_m$, i.e.

$$\left(\frac{\partial \hat{q}_k}{\partial x} \right)_{y=y_m} = 0, \quad (43)$$

or on the integral quantity

$$\int_0^\infty \hat{\mathbf{q}}^\dagger \frac{\partial \hat{\mathbf{q}}}{\partial x} dy = 0, \quad (44)$$

where the superscript \dagger refers to the complex conjugate. The auxiliary conditions enforce the variation of the shape function $\hat{\mathbf{q}}$ to remain small enough to justify the $(1/Re)$ scaling of $\partial \hat{\mathbf{q}}/\partial x$. At each streamwise position, the value of α is iterated such that auxiliary condition is satisfied.

4.3 Definition of growth

In the frame of the non-local theory, the physical growth rate, σ , of an arbitrary disturbance quantity ξ can be defined as

$$\sigma = -\alpha_i + \text{Re} \left\{ \frac{1}{\xi} \frac{\partial \xi}{\partial x} \right\}, \quad (45)$$

where the first RHS term is the contribution of the exponential part of the disturbance. The second term is the correction due to the changes of the amplitude function. Usually, ξ is taken to be a component of $\hat{\mathbf{q}}$, measured either at some fixed y or at the location where it reaches its maximum value. Moreover, the disturbance kinetic energy E , here defined as

$$E = \int_0^\infty (|\hat{u}|^2 + |\hat{w}|^2 + |\hat{v}|^2) dy,$$

can be used as a measure for the disturbance growth. Then, equation (45) becomes

$$\sigma = -\alpha_i + \frac{\partial}{\partial x} \ln(\sqrt{E}).$$

It should be noticed that the growth rate based on equation (45) can be a function of the normal coordinate, y .

The corresponding physical streamwise wavenumber is given by

$$\bar{\alpha} = \alpha_r + \text{Im} \left\{ \frac{1}{\hat{\xi}} \frac{\partial \hat{\xi}}{\partial x} \right\}, \quad (46)$$

The direction of wave propagation is given by the physical waveangle

$$\psi = \tan^{-1} \left(\frac{\beta}{\bar{\alpha}} \right). \quad (47)$$

The waveangle ψ also describes wave-front distortion or wave-ray curvature because ψ can vary both in the x - and y -directions.

4.4 Comparison with Direct Numerical Simulations

The most accurate stability results are those from Direct Numerical Simulations (DNS). A drawback of these methods is the long CPU time needed in such calculations, and the limitation to simple geometries. The comparisons of the DNS and non-local results over a wide range of Mach numbers have shown great potential of the non-local method for prediction of the stability characteristics as well as transition location.

Berlin et al. [70] calculated the neutral stability curves for two-dimensional disturbances in an incompressible flat plate boundary layer. Their results are given in figure 14. As can be seen there, a close agreement between the results from the DNS and non-local calculations is found. These results are also in good agreement with experimental data of Klingmann et al. [71]. The CPU time of the DNS calculations were about one hundred times larger than that of the PSE calculations.

4.5 Mathematical character of the PSE

Although no second x -derivatives of $\hat{\mathbf{q}}$ are present in (41), there is still some ellipticity in the stability equations. This is demonstrated by the rapid oscillations of the solutions when the marching step size becomes too small. This is illustrated in figure 15 for a Tollmien-Schlichting wave in a flat-plate boundary layer. The residual ellipticity is due to the upstream propagation through the pressure terms. The ill-posedness of the non-local stability equations has been studied by e.g., Haj-Hariri [72], Herbert [66], Li & Malik [73], Airiau [74]. Li & Malik showed that the dropping of $\partial \hat{p} / \partial x$ relaxes the step size restriction. They also gave the limit for the smallest stable step size to be $1/|\alpha_r|$. Andersson *et al.* [75] suggested the addition of a stabilizing term which is of the same order as the numerical errors. Then the modified equations are written as

$$\frac{\partial \hat{\mathbf{q}}}{\partial x} = L\hat{\mathbf{q}} + sL \frac{\partial \hat{\mathbf{q}}}{\partial x}. \quad (48)$$

This solution is derived for a first-order accurate backward Euler discretization of the PSE. In figure 16 the efficiency of this approach is demonstrated for instability waves in a rotating-disc boundary layer.

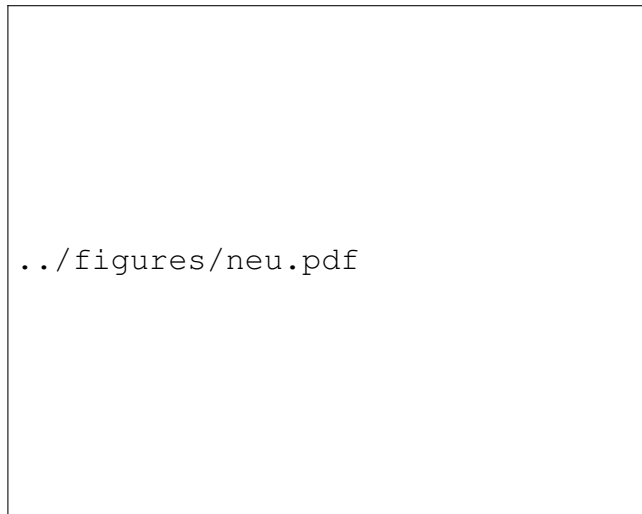


Fig. 14. Neutral stability curves based on the maximum of \hat{u} and \hat{v} . The non-local results are compared to the DNS calculations (Berlin et al. [70]) and experimental data (Klingmann et al. [71]).



Fig. 15. Effect of streamwise step size on the growth rates of $2D$ waves in a Blasius boundary layer flow, $F = 1.0 \times 10^{-4}$. Computed by `pse.m` with `stab=false`.

4.6 Tutorial on the PSE

The following exercises aim to provide an understanding of different aspects of PSE computations.

1. Familiarize yourself with the Matlab codes provided. The PSE are discretized using a Chebychev spectral discretization for wall-normal derivatives and a first- or second-order accurate backward Euler scheme for streamwise derivatives. Main program is called `pse.m`.
2. Choose a perturbation with a reduced frequency of $F = 2\pi f\nu^*/U_e^{*2} = \omega/Re = 10^{-4}$ and $\beta = 0$ and the computational domain $Re \in [400 - 1000]$ for the following computations. This should be done in the main code `pse.m`. The parameters to be set are `F`, `beta`, `Re` and `Re_end`. These parameters correspond to results presented in Figures 15 and 16.
3. Perform calculations for different step size Δx using `stab=false` and find the smallest stable solution and compare with the analytical value of $1/|\alpha_r|$. The step size can be changed by modifying the value of `Nstation`.
4. Perform calculations with a stable step size Δx using auxiliary conditions (43) and (44). This is

../figures/comp_step_stable.pdf

Fig. 16. Effect of stabilising term on the growth rates of $2D$ waves in a Blasius boundary layer flow, $F = 1.0 \times 10^{-4}$. Computed by `pse.m` with `stab=true`.

done but changing value of `iaux` from 1 (for integral norm) to 0. Verify that values of the physical growth rates and streamwise wavenumber $\bar{\alpha}$ are the same in both cases.

5. Study the function `integratePSE.m` and implementation of the stabilisation term given in (48). Run the code for different critical step sizes using `stab=true`. This implementation is correct for first-order backward Euler scheme (`FDorder='first'`).
6. Put a loop around the main program and run the code for different values of the reduced frequency to generate the neutral curves given in Figure 14. The data plotted in Figure 14 is found in the file `neu.dat`.

5 BiGlobal linear theory: the LNSE in 2D

When the base flow varies in two out of the three spatial directions and is independent of the third, $\bar{\mathbf{q}} = [\bar{u}, \bar{v}, \bar{w}, \bar{p}]^T(y, z)$, the analysis proceeds following the ansatz

$$\mathbf{q}(x, y, z, t) = \bar{\mathbf{q}}(y, z) + \boldsymbol{\varepsilon} \hat{\mathbf{q}}(y, z) e^{i[\alpha x - \omega t]} + c.c. \quad (49)$$

The disturbances are three-dimensional, but a harmonic dependence along the homogeneous x -direction is assumed, with the periodicity length $L_x = 2\pi/\alpha$. Upon substitution of (49) into the LNSE the system of equations results

$$i\alpha \hat{u} + \hat{v}_y + \hat{w}_z = 0, \quad (50)$$

$$\mathcal{L}_{2d} \hat{u} + \bar{u}_y \hat{v} + \bar{u}_z \hat{w} + i\alpha \hat{p} - i\omega \hat{u} = 0, \quad (51)$$

$$(\mathcal{L}_{2d} + \bar{v}_y) \hat{v} + \bar{v}_z \hat{w} + \hat{p}_y - i\omega \hat{v} = 0, \quad (52)$$

$$(\mathcal{L}_{2d} + \bar{w}_z) \hat{w} + \bar{w}_y \hat{v} + \hat{p}_z - i\omega \hat{w} = 0, \quad (53)$$

where $\mathcal{L}_{2d} = -(\partial_{yy} + \partial_{zz} - \alpha^2)/Re + i\alpha \bar{u} + \bar{v} \partial_y + \bar{w} \partial_z$.

Note that, if $\{.\}_z \equiv i\beta\{.\}$ is considered, the operators \mathcal{L}_{2d} and \mathcal{L}_{1d} become identical and the PDE-based system (50-53) reduces to the ODE-based system (13-16). The elliptic eigenvalue problem (50-53) is complemented with adequate boundary conditions for the disturbance variables, typically no-slip

on solid walls for the velocity components and the associated compatibility conditions for pressure, if the latter variable is maintained in the vector sought. Alternatively, pressure may be eliminated to yield the two-dimensional analogue of the Orr-Sommerfeld equation, as originally done by Tatsumi & Yoshimura [76], or the two-dimensional analogue of the Rayleigh equation, first presented and solved by Henningson [77].

Since the LNSE in two spatial dimensions can be reduced to the system of equations arising when only one inhomogeneous spatial direction exists, it is natural to pose two questions: (i) can (50-53) be used to predict parallel flow instability? (ii) when the assumptions underlying parallel flow theory are relaxed, can solution of (50-53) provide information inaccessible to solution of the classic Orr-Sommerfeld equation or absolute/convective instability analysis as applied to parallel or weakly non-parallel flows? Both questions were posed first in the context of adverse-pressure-gradient-generated laminar separation bubble in a flat plate boundary layer by Theofilis *et al.* [78], while in Blasius flow the same issues were addressed first by Åkervik *et al.* [79] and Rodríguez and Theofilis [80] and by several authors since.

Answers depended on the type of flow analysed. In the separated flow the discovery of the three-dimensional stationary amplified global mode of the laminar separation bubble [78] was only possible by application of global linear theory. On the other hand, in Blasius flow, imposition in a single BiGlobal computation of a given streamwise periodicity length and elimination of the wall-normal basic flow velocity component led to recovery of results identical to those delivered by multiple solutions of the Orr-Sommerfeld equation, each for a single streamwise wavenumber parameter. In other words, no information additional to that already contained in solutions of the classic one-dimensional linear instability analysis problem could be provided by application of global linear theory. However, relaxation of streamwise periodicity in the convectively unstable Blasius boundary layer in the context of a BiGlobal EVP solution poses the question of inflow/outflow boundary conditions appropriate for open flows; several choices are discussed by Rodríguez and Theofilis [80]. The branch(es) recovered in both related works [79,80] correspond to *stable* BiGlobal eigenmodes, while the location of the eigenspectra in (ω_r, ω_i) -space is strongly affected by the imposed inflow/outflow boundary conditions [80].

In the opinion of the authors, use of global linear theory is only justified when local modal analysis suggests that the flow will contain regions of local absolute instability. In that case, global linear theory can provide definitive answers which are free from the assumptions of local theory. However, when the instability in question is convective, classic linear instability analysis tools based on solution of the Orr-Sommerfeld equation not only are adequate from a physical point of view, but are also orders-of-magnitude more efficient than global linear theory.

5.1 Temporal BiGlobal stability

Temporal linear stability analysis may also be performed in the context of BiGlobal LST. The significance of the parameters α and ω appearing in (49) is analogous to that in local LST: α is a real wavenumber parameter, associated with a periodicity length along the (single) homogeneous spatial direction, x_1 , through $L = 2\pi/\alpha$ and is an input parameter for the analysis, as shown in (54). The box considered here is periodic only along the x_1 spatial direction, while the limiting case $\alpha = 0$ refers to two-dimensional perturbations superposed upon the two-dimensional basic state. The parameter ω is the sought complex eigenvalue, the real part of which, $\omega_r = \Re\{\omega\}$, is the eigenmode frequency, while its imaginary part, $\omega_i = \Im\{\omega\}$, is called the amplification rate of the perturbation if $\Im\{\omega\} > 0$, and the damping rate if $\Im\{\omega\} < 0$.

$$\tilde{\mathbf{q}} = \hat{\mathbf{q}}(y, z)e^{i(\alpha x - \omega t)} + c.c. = \hat{\mathbf{q}}(y, z)e^{i\alpha[x - (c_r + ic_i)t]} + c.c. \quad (54)$$

The primitive-variable formulation (50-53) can be written as a two-dimensional partial-derivative-based generalized eigenvalue problem, which can be recast in matrix form as the (linear) *temporal* BiGlobal eigenvalue problem,

$$\mathcal{A} \hat{\mathbf{q}} = \omega \mathcal{B} \hat{\mathbf{q}}. \quad (55)$$

Identification of a neutral stability curve is also the objective of BiGlobal linear theory and is also accomplished by projecting the amplification rate surface on the $\omega_i = 0$ plane. Common with the local theory, the flow Reynolds number (and Mach number, if compressible) is a flow parameter that needs to be varied. By contrast to local LST, here only one wavenumber parameter, α , exists. Also, the two-dimensional nature of the temporal eigenvalue problem to be solved makes it order(s) of magnitude more expensive than that governing local analysis. Alternative numerical methods need to be utilized for the solution of the BiGlobal EVP, which will be discussed next.

5.2 Spatial BiGlobal stability

In a global instability analysis context, most of the presently available literature has been performed in the temporal BiGlobal framework. However, the recent emergence of the PSE-3D concept gave rise to the associated necessity to initialize such computations using solutions of the spatial BiGlobal eigenvalue problem [81]. In this context, the significance of the parameter ω appearing in (7) is that of a real frequency, while the sought eigenvalue is now α , the real part of which is again associated with a periodicity length $L = 2\pi/\alpha_r$, while the imaginary part of this quantity, α_i , is the sought amplification/damping rate.

$$\tilde{\mathbf{q}} = \hat{\mathbf{q}}(y) e^{i[(\alpha_r + i\alpha_i)x + \beta z - \omega t]} + c.c. \quad (56)$$

The primitive-variable formulation (50-53) can also be written as a two-dimensional partial-derivative-based generalized eigenvalue problem, which can be recast in matrix form as the (nonlinear) *spatial* BiGlobal eigenvalue problem,

$$\mathcal{A} \hat{\mathbf{q}} = \sum_{k=1}^2 \alpha^k \mathcal{B}_k \hat{\mathbf{q}}. \quad (57)$$

The operators \mathcal{A} and \mathcal{B} defining (55) may be found explicitly in the literature, e.g. in Paredes *et al.* [81]. The nonlinearity (in α) of the eigenvalue problem (55) makes the size of the matrix discretizing the linear operator four times as large compared with that governing temporal BiGlobal instability when the companion matrix approach [82, 83] is used. A schematic of the size of the matrices governing local and global temporal and spatial instability analysis is shown in Figure 17. The efficient numerical solution of global eigenvalue problems in which the matrix is formed and stored is the subject of current research [84]. The neutral curve, which is identical to that obtained in a temporal BiGlobal context, is now obtained by projecting the amplification surface onto the $\alpha_i = 0$ plane.

5.3 2D EVP tutorials

5.3.1 The Helmholtz equation

Closer inspection of (50-53) reveals that the two-dimensional Laplace operator is at the heart of the operator \mathcal{L}_{2d} defining the BiGlobal direct and adjoint eigenvalue problems. When setting up a numerical

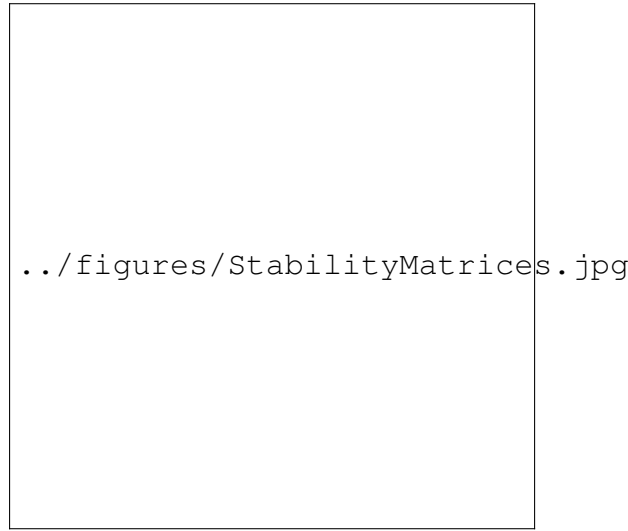


Fig. 17. Relative size of the discretized operators describing modal stability, when the same number of collocation nodes is used in one (local, PSE) and two (global, PSE-3D) resolved spatial directions (from de Tullio *et al.* [85]).

procedure for the solution of the BiGlobal EVP it is advisable to take advantage of partial validation cases, one of which is offered by the well-known (multi-dimensional) Helmholtz equation. The eigenvalue problem

$$\left(\frac{\partial^2}{\partial y^2} + \frac{\partial^2}{\partial z^2} \right) \phi + \lambda^2 \phi = 0 \quad (58)$$

in the rectangular membrane domain $y \in [0, L_y] \times z \in [0, L_z]$ is known to have an analytical solution [86] for the eigenvalues

$$\lambda_{n_y, n_z}^2 = \pi^2 \left[\left(\frac{n_y}{L_y} \right)^2 + \left(\frac{n_z}{L_z} \right)^2 \right]; \quad n_y, n_z = 1, 2, 3, \dots \quad (59)$$

and associated eigenfunctions

$$\phi_{n_y, n_z}(y, z) = \sin\left(\frac{\pi n_y y}{L_y}\right) \sin\left(\frac{\pi n_z z}{L_z}\right). \quad (60)$$

The eigenvalue problem (58-60) is therefore useful in assessing the accuracy of the proposed spatial discretization method, especially in the recovery of the higher eigenvalues/eigenfunctions, $n_y, n_z \gg 1$. Generating a solver for the two- and three-dimensional eigenvalue problems in a matrix-forming context requires the following steps:

1. Choose a spatial discretization method for each spatial direction.
 - (a) The spatial discretization method either can be different in each resolved spatial direction or can be the same, for example spectral collocation based on Chebyshev polynomials on the Gauss-Lobatto nodes (CGL). A typical situation in which different spatial discretizations should be used is the coupled resolution of wall-bounded and periodic directions, such as would occur when resolving Görtler or crossflow vortices on a flat-plate boundary layer. Here we will use the CGL method to set up the Laplacian operator.

2. Use of the Kronecker product to create the two- or three-dimensional matrix.
 - (a) The use of the Kronecker product is explained in section 6.3.1.
3. Impose boundary conditions.
 - (a) The imposition of boundary conditions can be made in a weak or a strong manner, respectively using basis functions which automatically satisfy boundary conditions (e.g. Fourier spectral collocation for periodic problems) or explicitly using rows of the matrix to impose Dirichlet or Neumann boundary conditions. Here we use strong imposition of boundary conditions.
4. Choose a direct or iterative eigenvalue solution procedure
 - (a) Matlab provides access to both methods, respectively through use of the **eig** and **eigs** routines.

The following tutorial exercises are recommended:

1. Familiarize yourself with aspects of the codes provided, such as Chebyshev collocation derivative matrices and the Kronecker product.

`set_y_grid.m`, `set_chebyshev_derivative_matrices.m`: set the Chebyshev Gauss-Lobatto collocation grid; form 1st and 2nd collocation derivative matrices.

`Helmholtz2d.m`: set up and solve the 2d Helmholtz EVP

`form_Helmholtz.m`: form the 2d Helmholtz EVP (58) using the collocation derivative matrices in the two spatial directions and the Kronecker product.

`impose_Helmholtz_BCs.m`: impose homogeneous Dirichlet boundary conditions on the discretized 2d Helmholtz operator.

`plot_Helmholtz2D.m`: plot selected eigenvalues and eigenfunctions of the 2d Helmholtz EVP

2. Run the script `Helmholtz2D.m` to obtain the spectrum of eigenvalue problem (58).
3. Plot the eigenfunctions of different modes to see their characteristic shape. Compare the eigenfunction corresponding to $\lambda/2\pi^2 = 34$ with that provided in figure 18.
4. Change the order of Chebychev polynomials and plot convergence of the leading members of the eigenspectrum.


5.3.2 Plane Poiseuille Flow

This tutorial introduces numerical solution of the BiGlobal eigenvalue problem by a matrix-forming tensor-product-based method. For simplicity, the equations solved are those to which (50-53) reduce when the two-dimensional perturbation limit is considered. Denoting the resolved spatial directions by x (streamwise) and y (wall-normal), the Linearised Navier-Stokes Equations can be written as a 3×3 matrix eigenvalue problem $Ax = \omega Bx$. Explicitly,

$$\begin{bmatrix} \mathcal{L} & -\bar{U}_y & -\partial_x \\ 0 & \mathcal{L} & -\partial_y \\ \partial_x & \partial_y & 0 \end{bmatrix} \begin{bmatrix} \hat{u} \\ \hat{v} \\ \hat{p} \end{bmatrix} = \omega \begin{bmatrix} I & 0 & 0 \\ 0 & I & 0 \\ 0 & 0 & 0 \end{bmatrix} \begin{bmatrix} \hat{u} \\ \hat{v} \\ \hat{p} \end{bmatrix}, \quad (61)$$

where $\mathcal{L} = 1/Re (\partial_{xx} + \partial_{yy}) - \bar{U}\partial_x$. In order for comparisons of results of the BiGlobal EVP with those of the Orr-Sommerfeld equation to be possible, the assumptions underlying local analysis are made, namely that flow is parallel and has a single streamwise velocity component, $U(y)$. This permits taking the streamwise spatial direction x to be homogeneous and resolve it using Fourier collocation [87].

A convenient geometry in which these ideas can be demonstrated is the plane channel, the eigenspectrum of which is known from section 2.9 and figure 10. By contrast to local theory, here streamwise



```
../Figures/Poisson2D_EF34.pdf
```

Fig. 18. The eigenvector corresponding to $(\lambda/\pi)^2 = 34$ in the solution of (59). Shown are five isolines between zero and maximum (solid line) and between minimum and zero (dashed line).

periodicity is imposed implicitly through the choice of a streamwise periodicity length, L_x , which corresponds to a wavenumber $\alpha = 2\pi/L_x$ and its harmonics. Spectral collocation based on the Chebyshev Gauss-Lobatto nodes is used to discretize the wall-normal spatial direction. The Kronecker product discussed in 6.3.1 is used to form the two-dimensional matrices A and B .

The following tutorial exercises are recommended:

1. Familiarize yourself with Fourier spectral discretization in the code provided
`set_x_grid.m`, `set_fourier_derivative_matrices.m`: set the Fourier collocation grid; form 1st and 2nd collocation derivative matrices.
`map_x.m`: linearly transform the Fourier system.
`calculate_ddx.m`: compute Fourier collocation derivative of an 1D periodic function
`EVP2d.m`: set up and solve the 2d BiGlobal EVP
`form_EVP2d.m`: form the 2d EVP using the collocation derivative matrices in the two spatial directions, using Fourier spectral collocation along x , Chebyshev collocation based on the Gauss-Lobatto points along y and the Kronecker product.
`impose_BCs.m`: impose boundary conditions (along y) on the discretized LNSE operator.
`plot_EVP2d.m`: plot selected eigenvalues and eigenfunctions of the 2d BiGlobal EVP
2. Run the code `EVP2d.m` to obtain the eigenspectrum of (61). Verify that it is identical with that shown in Fig. 10. The amplitude functions corresponding to the unstable Tollmien-Schlichting (TS) mode and those of the least damped member of the P family are shown in Fig. 19. The eigenfunctions of the TS mode correspond exactly to those obtained by local analysis and shown as one-dimensional amplitude functions in Fig. 11.
3. Using the code provided, perform calculations for different values of the Reynolds number, Re , using a streamwise periodicity length, $L_x = 2\pi$. Try $Re = 5772$ and $Re = 7500$ and compare your results with those obtained by solving the Orr-Sommerfeld equation in which $\alpha = 2\pi/L_x$ is explicitly imposed [39, 87].
4. Modify the code provided to solve the 2d EVP for the Blasius boundary layer. The 3×3 system is still solved, but you need to modify the wall-normal domain, including a mapping function, as well as the base flow (and its derivatives!) to include both a streamwise, $\bar{U}(x, y)$, and a wall-normal,



Fig. 19. Amplitude functions corresponding to the unstable Tollmien-Schlichting mode (left column) and the least stable eigenmode member of the P family (right column) in PPF flow at $Re = 10^4$, $\alpha = 1$. Upper to lower rows: $\hat{u}(x, y)$, $\hat{v}(x, y)$ and $\hat{p}(x, y)$.

$\bar{V}(x, y)$, velocity component. Use the boundary layer displacement thickness as length scale to reproduce the near-critical conditions of Mack [88]: $Re = 998$, $\alpha = 0.309$; at those parameters $\omega = 0.36412129 + 0.00796250i$ [89]. Compare the eigenfunctions with those shown by Akervik *et al.* [90].

5. Extend the code provided to solve the full (4×4) system (50-53), including spanwise flow perturbations. Use the rectangular duct to test your code and references [76, 91] to compare your results.

6 Numerical Solution Methods

6.1 One-dimensional eigenvalue problems

The solution of the eigenvalue problems introduced in the previous sections implies two steps: spatial discretization, which converts the linear operators associated with the temporal or spatial EVPs to linear or nonlinear matrix eigenvalue problems, respectively; and solution of the latter using an appropriate algorithm.

Spatial discretization may be performed using spectral methods, e.g. collocation based on the Chebyshev Gauss-Lobatto points, finite-difference methods, ranging from standard second-order centered to compact [92], Dispersion Relation Preserving (DRP) [93] or stable very high-order finite differences of order q (FD- q) [84, 94], low-order finite-element or high-order spectral-element [95] methods; see [12] for further details.

As far as the solution of the matrix eigenvalue problem is concerned, the QZ algorithm [96] can be used for this one-dimensional eigenvalue problem. Although the memory and runtime requirements of this algorithm scale with the square and the cube of the matrix leading dimension, respectively, modern hardware can easily deliver converged solutions of at least the most interesting leading eigenmodes. When the leading dimension becomes rather large, e.g. in case of secondary instability analysis in which several Floquet coefficients need be calculated in a coupled manner, iterative algorithms for the recovery of the leading eigenvalues come into consideration. Such algorithms will be outlined in the context of global stability analysis.

In practical terms, the linear algebra work is undertaken using software packages such as the Open



./Figures/FDq_vs_ALL.pdf

Fig. 20. Relative error in the computation of the leading eigenmode in PPF at $Re = 10^4$, $\alpha = 1$, using spectral collocation (black solid line), a suite of common high-order finite-difference methods (blue lines) and the recently proposed FD-q finite-difference method.

Source LAPACK library, or proprietary packages which are equivalent in terms of their functionality as far as the solution of the problems at hand is concerned, such as the cross-platform NAG[®] library or the platform-specific Intel MKL[®] or the IBM ESSL[®] linear algebra software.

Finally, Matlab can be used in order to obtain both the entire eigenspectrum, using the direct approach, or the most interesting part of it, employing iterative means.

Figure 20 shows a comparison between results for the relative error in the leading eigenvalue of plane Poiseuille flow (PPF) at $Re = 10^4$, $\alpha = 1$, obtained using the classic spectral method of Orszag [39] and a suite of the above mentioned high-order finite difference methods. It can be seen that, at the same order of accuracy, the FD-q method [84] outperforms all of its peers: a preset level of accuracy, denoted as ϵ_ω in this figure, is arrived at earlier in terms of number of discretization nodes, N , when use of the FD-q method is made as opposed to any of the standard high-order finite-difference methods, Padé, SBP or DRP methods. Conversely, if a given level of discretization is available, indicated by a constant value of the number of discretization nodes, N , in the figure, the relative error in the FD-q approximation is substantially smaller than that in any of its peers. When the order q increases, the results of the FD-q method converge toward those of the spectral method, albeit using banded matrix discretization of the operator. This offers the potential to use sparse linear algebra operations without sacrificing accuracy, which makes the FD-q method an excellent candidate to discretize the linearized Navier–Stokes operator in higher spatial dimensions.

6.2 Two- and three-dimensional eigenvalue problems

The solution of a multi-dimensional eigenvalue problem also implies two steps: spatial discretization, which converts the linear operator into a linear or nonlinear matrix eigenvalue problem; and solution of the latter using an appropriate (typically iterative) algorithm.

The same spatial discretization method used for local analysis may also be used for the 2D (or 3D) eigenvalue problem. Spectral collocation based on the Chebyshev Gauss-Lobatto points, finite-difference, finite-volume, finite-element and spectral-element methods have all been employed in this context.

6.3 Matrix-forming vs. time-stepping

A dichotomy exists in terms of solving the multi-dimensional eigenvalue problem by extending the techniques used in local stability analysis and forming a multi-dimensional matrix “matrix-forming”) or by downsizing and expanding a direct numerical simulation algorithm to obtain solutions to the multi-dimensional (direct or adjoint) EVP by ”time-stepping” techniques. A short critical discussion of advantages and disadvantages of either methodology follows.

The main advantages of the matrix-forming approach rely in programming simplicity and flexibility. Given an one-dimensional differentiation matrix $D \in C^{m \times n}$ it is straightforward to form any of the linear one-dimensional operators discussed in this paper. In two or three spatial dimensions the Kronecker product of matrices, to be introduced shortly, can be used. An additional key advantage of a matrix-forming approach is its flexibility: incompressible or compressible, viscous or inviscid operators may be programmed in a straightforward manner into the same code, thus minimizing the amount of validation and verification work necessary when a new problem is to be tackled. The main disadvantage of the matrix-forming approach is the *curse of dimensionality* associated with matrix storage and inversion. If $1 \leq m \leq 5$ is the number of equations that need be solved, memory and CPU time requirements for direct matrix operations scale as shown in Table 2.

	memory	CPU time
1D:	$O((mn)^2)$	$O((mn)^3)$
2D:	$O((mn)^4)$	$O((mn)^6)$
3D:	$O((mn)^6)$	$O((mn)^9)$

Table 2. Memory and CPU time requirements for dense-matrix operations in LST

The theoretical scalings shown in Table 2 are encountered in numerical solutions of eigenvalue problems described by dense matrices. Treating the matrix as dense is the only option when spectral discretization of the spatial LNSE operator is employed. Use of alternative spatial discretization methods, which result in banded or sparse matrices, permits reducing the high cost of direct inversion shown in Table 2 through the use of sparse matrix linear algebra. As an example, the FD-q methods discussed earlier result in the following scalings

$$\text{Mem}_{\text{sparse}} = \left(\frac{q+1}{N+1} \right)^a \times \text{Mem}_{\text{dense}} \quad (62)$$

and

$$\text{Time}_{\text{sparse}} = \left(\frac{q+1}{N+1} \right)^b \times \text{Time}_{\text{dense}}, \quad (63)$$

with $a \approx 2.7$ and $3 \leq b \leq 4$ for $8 \leq q \leq 24$, determined empirically [84]. This gives the high-order finite-difference method a strong competitive advantage over the spectral spatial discretization of the multi-dimensional EVP.

When use of matrix formation is prohibitively expensive, the alternative time-stepping approach may be used. No memory availability or memory management issues are present in the time-stepping methodology, since operations are performed in the same manner as those of the underlying DNS code used.

Relatively minor code modifications are required; steady and time-periodic flows may be analysed with one code which may time-advance either the LNSE or the full Navier–Stokes equations. On the other hand, the flexibility of the matrix-forming approach is lost and every time one needs to solve a different stability problem, an appropriate (validated) DNS code needs to be available. Incompressible and compressible flow instability problems need to be treated separately. More subtly, the length of time-integration in a time-stepping algorithm is *a-priori* unknown, while the efficiency of the method is progressively lost with increasing m_{Kryl} , the dimension of the subspace in which the eigenvalue problem is projected. Only the matrix-forming approach will be discussed in this article; an extensive discussion of both approaches may be found in [12].

6.3.1 The Kronecker product

A key element in the matrix-forming approach in two spatial dimensions is the Kronecker product, $M \equiv A \otimes B$, where matrices $A \in \mathbb{C}^{m \times n}$ and $B \in \mathbb{C}^{r \times s}$ represent discretization in either of the two spatial directions. Then $M \in \mathbb{C}^{mr \times ns}$ discretizes in both dimensions in a coupled manner and is defined as

$$M \equiv A \otimes B = \begin{pmatrix} a_{11}B & a_{12}B & \cdots & a_{1n}B \\ a_{21}B & a_{22}B & \cdots & a_{2n}B \\ \vdots & \vdots & \ddots & \vdots \\ a_{m1}B & a_{m2}B & \cdots & a_{mn}B \end{pmatrix}. \quad (64)$$

The extension to three spatial dimensions is straightforward. However, note that the dimensions of the two-dimensional matrix M are now $mr \times ns$, which all but precludes using direct methods based on the QZ algorithm for the recovery of its eigenvalues. The most used alternative for the computation of an interesting subset of eigenvalues in multiple spatial dimensions is based on subspace iteration, notably the Arnoldi algorithm. However, before introducing this algorithm, some thoughts on the properties of matrix M are appropriate.

6.3.2 Sparsity patterns in global instability analysis

The nature of the global eigenvalue problem to be solved determines the choice of both spatial discretization and EVP solution approach to be followed. In this respect, it is instructive to examine the sparsity pattern of relevant discretized linear operators. Figure 21 shows these patterns (obtained using the *"spy"* function of Matlab) for the Laplacian, the incompressible BiGlobal eigenvalue problem in a two-component basic flow (the lid-driven cavity [97]) and the compressible BiGlobal eigenvalue problem pertinent to a three-component basic flow (the swept leading edge boundary layer [98]). All three problems have been discretized using the spectral collocation method based on the Chebyshev Gauss-Lobatto grid, which will be outlined in the next section, and have been plotted using the same scale, in order for relative differences to be appreciated.

The first point concerns the symmetric nature of the Laplacian, as opposed to the non-symmetric nature of both of the other two problems, which is immediately obvious in figure 21. This is a key consideration when choosing an algorithm for the solution of the EVP: what will work nicely for the Laplace/Poisson/Helmholtz EVP may not converge as rapidly or not work at all for the global stability problem. Interestingly, if the SVD of the stability matrix is sought, then the symmetry property may be recovered and methods for the Laplace equation may also be employed.

The second point to be made is that the sparsity pattern of the global EVP is affected by two factors, whether incompressible or compressible flow instability is monitored, and whether (two-dimensional) one-, two- or three-component flow instability is addressed. While a rather large number of zero elements may be seen in the analysis of a single basic flow velocity component in incompressible flow

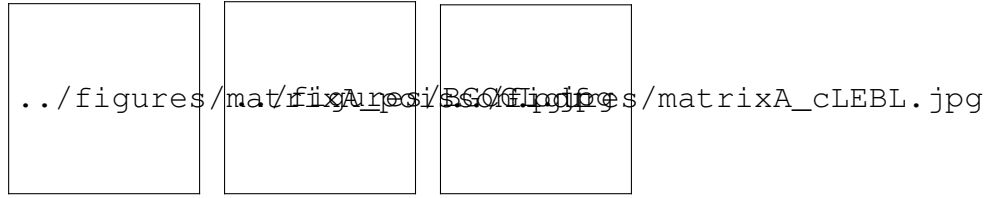


Fig. 21. Sparsity patterns of the Laplace operator (left) incompressible BiGlobal EVP (middle) and compressible BiGlobal EVP (right), discretized using the spectral collocation method.

(e.g. the rectangular duct [76]), the non-zero elements predominate when global instability analysis of compressible flow is performed, in which all three velocity components are present (e.g. the swept leading edge boundary layer [98]). Consequently, sparse linear algebra software which performs nicely for the former may become uncompetitive for the latter class of problems, for which the computing cost of the solution approaches that of a dense approach.

This leads naturally to the last and probably most significant point that can be deduced from the results presented: if the matrix-forming approach is to be made competitive to other methodologies for the solution of the global EVP, the sparsity pattern needs to be increased substantially. This could be achieved by substituting the spectral collocation approach with a low-order finite-difference method. However, the loss of accuracy of the finite-difference method would not compensate for the increase of efficiency. What is really needed is a finite-difference method which is (very) high-order accurate (and stable) and at the same time requires much shorter stencils than those used in the spectral collocation approach. Such a method has been introduced by Paredes *et al.* [84], to which the reader is referred for details.

6.3.3 On iterative solutions of the EVP - the Arnoldi algorithm

By far the widest-employed and most successful approach for numerical solution of large-scale eigenvalue problems is the Arnoldi [99, 100] member of the Krylov subspace iteration methods. One of the variants of the Arnoldi algorithm [28] converts the generalized EVP (55) into the standard eigenvalue problem

$$\hat{\mathbf{A}}\hat{\mathbf{q}} = \mu\hat{\mathbf{q}}, \quad \hat{\mathbf{A}} = (\mathbf{A} - \sigma\mathbf{B})^{-1}\mathbf{B}, \quad \mu = \frac{1}{\omega - \sigma} \quad (65)$$

and constructs a Krylov subspace, a Hessenberg matrix H_{ij} and a sequence of Ritz vectors in an iterative manner, as schematically shown in figure 22. The eigenvalues of the (much smaller, compared with the original problem dimension) Hessenberg matrix may be calculated by direct means using the QZ algorithm and are increasingly better approximations of those of the original problem as the Krylov subspace dimension increases.

Acknowledgement

The second author thanks David Tempelmann for providing some of the Matlab codes used in the PSE tutorial.

../figures/FromPrAeS2003.pdf

Fig. 22. The Arnoldi algorithm (from [28])

References

- [1] Schmid, P. J., and Brandt, L., 2013. “Analysis of fluid systems: stability, receptivity, sensitivity”. *Appl. Mech. Rev.*
- [2] Barkley, D., 2006. “Linear analysis of the cylinder wake mean flow”. *Europhys. Lett.*, **75**, pp. 750–756.
- [3] Sipp, D., and Lebedev, A., 2007. “Global stability of base and mean flows: a general approach and its applications to cylinder and open cavity flows”. *J. Fluid Mech.*, **593**, pp. 333–358.
- [4] Åkervik, E., Brandt, L., Henningson, D. S., Høpfner, J., Marxen, O., and Schlatter, P., 2006. “Steady solutions of the NavierStokes equations by selective frequency damping”. *Phys. Fluids*, **18**, p. 068102.
- [5] Kleiser, L., and Zang, T. A., 1991. “Numerical simulation of transition in wall-bounded shear flows”. *Annu. Rev. Fluid Mech.*, **23**, pp. 495–537.
- [6] Fasel, H., Rist, U., and Konzelmann, U., 1990. “Numerical investigation of the three-dimensional development in boundary layer transition”. *AIAA J.*, **28** (1), pp. 29–37.
- [7] Lundbladh, A., Henningson, D. S., and Johansson, A. V., 1992. An efficient spectral integration method for the solution of the Navier-Stokes equations. FFA-TN 1992-28, Aeronautical Research Institute of Sweden, Bromma.
- [8] Lin, C. C., 1955. *Theory of hydrodynamic stability*. Cambridge University Press.
- [9] Drazin, P. G., and Reid, W. H., 1981. *Hydrodynamic Stability*. Cambridge University Press.
- [10] Mack, L. M., 1984. Boundary layer stability theory: Special course on stability and transition of laminar flow. AGARD Report 709, Paris, France.
- [11] Th. Herbert, 1997. “Parabolized stability equations”. *Ann. Rev. Fluid Mech.*, **29**, pp. 245–283.
- [12] Theofilis, V., 2011. “Global linear instability”. *Annu. Rev. Fluid Mech.*, **43**, pp. 319–352.
- [13] Rayleigh, J. W., 1898. *The Theory of Sound*, Vol. 1 & 2. Dover.
- [14] Drazin, P., and Reid, W., 1981. *Hydrodynamic Stability*. Cambridge University Press.
- [15] Smith, A. M. O., and Gamberoni, N., 1956. Transition, pressure gradient and stability theory. Tech. Rep. ES 26388, Douglas Aircraft Co.
- [16] van Ingen, J. L., 1956. A suggested semi-empirical method for the calculation of the boundary layer transition region. Report VTH-74, Univ. of Technology, Dep. of Aero. Eng., Delft.
- [17] Arnal, D., 1993. Boundary layer transition: Predictions based on linear theory. Special course on ‘progress in transition modeling’, March-April 1993, AGARD-R-793. 2-1-2-63.
- [18] Morkovin, M. V., 1969. “The many faces of transition.”. In *Viscous Drag Reduction*, C. S. Wells, ed. Plenum Press.
- [19] Reshotko, E., 1976. “Boundary-layer stability and transition.”. *annrev*, **8**, pp. 311–350.
- [20] Crouch, J. D., 1992. “Non-localized receptivity of boundary layers”. *J. Fluid Mech.*, **244**,

pp. 567–581.

- [21] Saric, W., Reed, H., and Kerschen, E., 2000. “Boundary-layer receptivity to freestream disturbances”. *Annu Rev Fluid Mech*, **34**, pp. 291–319.
- [22] Pralits, J. O., Airiau, C., Hanifi, A., and Henningson, D. S., 2000. “Sensitivity analysis using adjoint parabolized stability equations for compressible flows”. *Flow, turbulence and combustion*, **65**(3), pp. 321–346.
- [23] Tempelmann, D., Schrader, L.-U., Hanifi, A., Brandt, L., and Henningson, D. S., 2012. “Swept wing boundary-layer receptivity to localized surface roughness”. *Journal of Fluid Mechanics*, **711**, pp. 516–544.
- [24] Zuccher, S., and Luchini, P. “Boundary-layer receptivity to external disturbances using multiple scales”. *Meccanica*, pp. 1–27.
- [25] Huerre, P., and Monkewitz, P. A., 1990. “Local and global instabilities in spatially developing flows”. *Annu. Rev. Fluid Mech.*, **22**, pp. 473–537.
- [26] Huerre, P., and Rossi, M., 1998. “Hydrodynamic instabilities in open flows”. In *Hydrodynamics and nonlinear instabilities*, C. Godreche and P. Manneville, eds. Cambridge University Press.
- [27] Huerre, P., and Monkewitz, P. A., 2000. “Open shear flow instabilities”. In *Perspectives in Fluid Dynamics : A Collective Introduction to Current Research*, G. K. Batchelor, H. K. Moffat, and M. G. W. C.U.P., eds. Cambridge University Press.
- [28] Theofilis, V., 2003. “Advances in global linear instability analysis of nonparallel and three-dimensional flows”. *Prog. Aero. Sci.*, **39**, pp. 249–315.
- [29] Mack, L. M., 1984. “Boundary-layer stability theory”. In AGARD Report, no. 709, pp. 3–1–3–8.
- [30] Schmid, P., and Henningson, D. S., 2001. *Stability and Transition in Shear Flows*. Springer, New York.
- [31] Fedorov, A., 2011. “Transition and stability of high-speed boundary layers”. *Annu. Rev. Fluid Mech.*, **43**, pp. 79–95.
- [32] Zhong, X., and Wang, X., 2012. “Direct numerical simulation on the receptivity, instability, and transition of hypersonic boundary layers”. *Annu. Rev. Fluid Mech.*, **44**, pp. 527–561.
- [33] Yu, M.-H., and Monkewitz, P. A., 1990. “The effect of nonuniform density on the absolute instability of two-dimensional inertial jets and wakes”. *Phys Fluids A*, **2**(7), pp. 1175–1181.
- [34] Juniper, M. P., 2007. “The full impulse response of two-dimensional shear flows and implications for confinement”. *J. Fluid Mech.*, **590**, pp. 163–185.
- [35] Rees, S. J., and Juniper, M. P., 2009. “The effect of surface tension on the stability of unconfined and confined planar jets and wakes”. *J. Fluid Mech.*, **633**, pp. 71–97.
- [36] Healey, J. J., 2006. “A new convective instability of the rotating-disk boundary layer with growth normal to the plate”. *J. Fluid Mech.*, **560**, pp. 279–310.
- [37] Gaster, M., 1962. “A note on the relation between temporally-increasing and spatially-increasing disturbances in hydrodynamic stability”. *J. Fluid Mech.*, **14**, pp. 222–224.
- [38] Huerre, P., and Monkewitz, P. A., 1990. “Local and global instabilities in spatially developing flows”. *Ann. Rev. Fluid Mech.*, **22**, pp. 473–537.
- [39] Orszag, S. A., 1969. Numerical methods for the simulations of turbulence. *Phys. of Fluids Supplement II*.
- [40] Kirchner, N., 2000. “Computational aspects of the spectral galerkin fem for the orr-sommerfeld equation”. *Int. J. Numer. Meth. Fluids*, **32**, pp. 119–137.
- [41] Michalke, A., 1964. “On the inviscid instability of the hyperbolic-tangent velocity profile”. *J. Fluid Mech.*, **19**, pp. 543–556.
- [42] Herbert, T., 1984. “Secondary instability of shear flows”. In AGARD–R–709 Special Course on Stability and Transition of Laminar Flow, pp. 7.1–7.13.
- [43] Herbert, T., 1984. “Analysis of the subharmonic route to transition in boundary layers.”.

- [44] Herbert, T., 1988. “Secondary instability of boundary layers”. *Annu. Rev. Fluid Mech.*, **20**, pp. 487–526.
- [45] Kachanov, Y. S., and Levchenko, V. Y., 1984. “The resonant interaction of disturbances at laminar-turbulent transition in a boundary layer”. *J. Fluid Mech.*, **138**, pp. 209–47.
- [46] Kachanov, Y. S., 1994. “Physical mechanisms of laminar-boundary-layer transition”. *Annu. Rev. Fluid Mech.*, **26**, pp. 411–482.
- [47] Orszag, S. A., and Patera, A. T., 1983. “Secondary instability of wall-bounded shear flows”. *J. Fluid Mech.*, **128**, pp. 347–385.
- [48] Herbert, T., 1991. Boundary-layer transition - analysis and prediction revisited. AIAA Paper 91-0737.
- [49] Saric, W. S., and Thomas, A. S. W., 1984. “Experiments on the subharmonic route to turbulence in boundary layers”. T. Tatsumi, ed., Vol. Turbulence and Chaotic Phenomena in Fluids, North-Holland, pp. 117–122.
- [50] Herbert, T., 1983. “Secondary instability of plane channel flow to subharmonic three dimensional disturbances”. *Phys. Fluids*, **26**, pp. 871–874.
- [51] Bouthier, M., 1972. “Stabilité linéaire des écoulements presque parallèles”. *Journal de Mécanique*, **11**, pp. 599–621.
- [52] Gaster, M., 1975. “A theoretical model for the development of a wave packet in a laminar boundary layer”. *Proc. Roy. Soc. Lond. Ser. A*, **347**, pp. 271–289.
- [53] Saric, W. S., and Nayfeh, A. H., 1975. “Non-parallel stability of boundary layer flows”. *Phys. Fluids*, **18**, pp. 945–950.
- [54] Gaponov, S. A., 1981. “The influence of flow non-parallelism on disturbance development in the supersonic boundary layers”. In Proceedings of the 8-th Canadian Congress of Applied Mechanics, pp. 673–674.
- [55] El-Hady, N., 1991. “Nonparallel instability of supersonic and hypersonic boundary layers”. *Phys. Fluids A*, **3**, pp. 2164–2178.
- [56] Hall, P., 1983. “The linear development of görtler vortices in growing boundary layers”. *J. Fluid Mech.*, **130**, pp. 41–58.
- [57] Itoh, N., 1981. “Secondary instability of laminar flows”. *Proc. Roy. Soc. Lond. Ser. A*, **375**, pp. 565–578.
- [58] Herbert, T., and Bertolotti, F. P., 1987. “Stability analysis of nonparallel boundary layers”. *Bull. Am. Phys. Soc.*, **32**, p. 2079.
- [59] Bertolotti, F. P., Herbert, T., and Spalart, S., 1992. “Linear and nonlinear stability of the Blasius boundary layer”. *J. Fluid Mech.*, **242**, pp. 441–474.
- [60] Simen, M., 1992. “Local and non-local stability theory of spatially varying flows”. In *Instability, Transition and Turbulence*, M. Hussaini, A. Kumar, and C. Streett, eds. Springer, pp. 181–201.
- [61] Andersson, P., Berggren, M., and Henningson, D., 1998. “Optimal disturbances and bypass transition in boundary layers”. *Phys. Fluids*. (Submitted).
- [62] Luchini, P., 1996. “Reynolds number independent instability of the Blasius boundary layer over a flat surface”. *J. Fluid Mech.*, **327**, pp. 101–115.
- [63] Tempelmann, D., Hanifi, A., and HENNINGSON, D., 2010. “Spatial optimal growth in three-dimensional boundary layers”. *Journal of Fluid Mechanics*, **646**, p. 5.
- [64] Tempelmann, D., Hanifi, A., and Henningson, D. S., 2012. “Spatial optimal growth in three-dimensional compressible boundary layers”. *Journal of Fluid Mechanics*, **704**, p. 251.
- [65] Bertolotti, F. P., 1991. “Linear and nonlinear stability of boundary layers with streamwise varying properties.”. PhD thesis, The Ohio State University, Department of Mechanical Engineering, Columbus, Ohio.
- [66] Herbert, T., 1994. Parabolized stability equations. Tech. Rep. 793, AGARD.

- [67] Hanifi, A., Henningson, D., Hein, S., Bertolotti, F. P., and Simen, M., 1994. Linear nonlocal instability analysis - the linear nolot code. Tech. Rep. FFA TN 1994-54, FFA. See also Hein *et al.* [68].
- [68] Hein, S., Bertolotti, F. P., Simen, M., Hanifi, A., and Henningson, D. S., 1994. Linear non-local instability analysis - the linear NOLOT code. Tech. Rep. DLR-IB 223-94 A 43, Deutsche Forschungsanstalt für Luft- und Raumfahrt.
- [69] Bertolotti, F. P., Herbert, T., and Spalart, S. P., 1992. “Linear and nonlinear stability of the blasius boundary layer”. *J. Fluid Mech.*, **242**, pp. 441–474.
- [70] Berlin, S., Hanifi, A., and Henningson, D. S., 1998. The neutral stability curve for non-parallel boundary layer flow. in *Oblique Waves in Boundary layer Transition*, Ph.D. Thesis, Royal Institute of Technology, Stockholm.
- [71] Klingmann, B. G. B., Boiko, A. V., Westin, K. J. A., Kozlov, V. V., and Alfredsson, P. H., 1993. “Experiments on the stability of tollmien-schlichting waves”. *Eur. J. Mech., B/Fluids*, **12**, pp. 493–514.
- [72] Haj-Hariri, H., 1994. “Characteristics analysis of the parabolized stability equations”. *Stud. Appl. Math.*, **92**, pp. 41–53.
- [73] Li, F., and Malik, M. R., 1995. “Mathematical nature of parabolized stability equations”. In *Laminar-Turbulent Transition*, R. Kobayashi, ed., Springer-Verlag, pp. 205–212.
- [74] Airiau, C., 1994. “Linear and weakly nonlinear stability of an incompressible laminar boundary layer by the parabolized stability equations (PSE)”. PhD thesis, L’École Nationale Supérieure de l’Aéronautique et de l’Espace.
- [75] Andersson, P., Henningson, D. S., and Hanifi, A., 1998. “On a stabilization procedure for the parabolic stability equations”. *J. Eng. Math.*, **33**, pp. 311–332.
- [76] Tatsumi, T., and Yoshimura, T., 1990. “Stability of the laminar flow in a rectangular duct”. *J. Fluid Mech.*, **212**, pp. 437–449.
- [77] Henningson, D. S., 1987. Stability of parallel inviscid shear flow with mean spanwise variation. Tech. Rep. TN 1987-57, FFA.
- [78] Theofilis, V., Hein, S., and Dallmann, U., 2000. “On the origins of unsteadiness and three-dimensionality in a laminar separation bubble.”. *Phil. Trans. Roy. Soc. London (A)*, **358**, pp. 3229–324.
- [79] Åkervik, E., Ehrenstein, U., Gallaire, F., and Henningson, D. S., 2008. “Global two-dimensional stability measures of the flat plate boundary-layer flow”. *Eur. J. Mech. B/ Fluids*, **27**(5), pp. 501–513.
- [80] Rodríguez, D., and Theofilis, V., 2008. “On instability and structural sensitivity of incompressible laminar separation bubbles in a flat-plate boundary layer”. AIAA Paper 2008-4148.
- [81] Paredes, P., Theofilis, V., Rodríguez, D., and Tendero, J. A., 6th AIAA Theoretical Fluid Mechanics Conference, Honolulu, Hawaii, June 27-30, 2011. “The pse-3d instability analysis methodology for flows depending strongly on two and weakly on the third spatial dimension”. No. AIAA Paper 2011-3752.
- [82] Bridges, T., and Morris, P., 1984. “Differential eigenvalue problems in which the parameter appears nonlinearly”. *Journal of Computational Physics*, **55**, pp. 437–460.
- [83] Theofilis, V., 1995. “Spatial stability of incompressible attachment line flow”. *Theor. Comput. Fluid Dyn.*, **7**, pp. 159–171.
- [84] Paredes, P., Hermanns, M., Clainche, S. L., and Theofilis, V., 2013. “O(10⁴) speedup in global linear instability analysis using matrix formation”. *Comput. Meth. Appl. Mech. Eng.*, **253**, pp. 287 – 304.
- [85] de Tullio, N., Paredes, P., Sandham, N. D., and Theofilis, V., 2013. “Roughness-induced instability and breakdown to turbulence in a supersonic boundary-layer”. *J. Fluid Mech.*, p. (submitted).

- [86] Morse, P. M., and Feshbach, H., 1953. *Methods of Theoretical Physics, Parts I, II*. McGraw-Hill.
- [87] Canuto, C., Hussaini, M. Y., Quarteroni, A., and Zang, T. A., 1987. *Spectral methods in fluid dynamics*. Springer.
- [88] Mack, L. M., 1976. “A numerical study of the temporal eigenvalue spectrum of the Blasius boundary layer”. *J. Fluid Mech.*, **73**, pp. 497–520.
- [89] Theofilis, V., 1994. “The discrete temporal eigenvalue spectrum of the generalised hiemenz flow as solution of the orr-sommerfeld equation”. *J. of Engineering Mathematics*, **28**, pp. 241–259.
- [90] Akervik, E., Ehrenstein, U., Gallaire, F., and Henningson, D. S., 2008. “Global two-dimensional stability measures of the flat plate boundary-layer flow”. *Eur. J. Mech. B / Fluids*, **27**(5), pp. 501–513.
- [91] Theofilis, V., Duck, P. W., and Owen, J., 2004. “Viscous linear stability analysis of rectangular duct and cavity flows”. *J. Fluid. Mech.*, **505**, pp. 249–286.
- [92] Lele, S., 1992. “Compact finite difference schemes with spectral- like resolution”. *Journal of Computational Physics*, **103**, pp. 16–42.
- [93] Tam, C., and Webb, J., 1993. “Dispersion-relation-preserving finite-difference schemes for computational acoustics”. *J. Comp. Phys.*, **107**(2), pp. 262–281.
- [94] Hermanns, M., and J.A., H., 2008. “Stable high-order finite-difference methods based on non-uniform grid point distributions”. *International Journal for Numerical Methods in Fluids*, **56**, pp. 233–255.
- [95] Karniadakis, G. E., and Sherwin, S. J., 2005. *Spectral/hp element methods for Computational Fluid Dynamics (2nd ed.)*. Oxford University Press.
- [96] Golub, G. H., and van Loan, C. F., 1996. *Matrix Computations*, 3 ed. The Johns Hopkins University Press.
- [97] Theofilis, V., AIAA-2000-1965. “Globally unstable basic flows in open cavities”. *6th AIAA Aeroacoustics Conference and Exhibit*.
- [98] Theofilis, V., Fedorov, A., and Collis, S. S., 2006. “Leading-edge boundary layer flow: Prandtl’s vision, current developments and future perspectives”. In *One hundred years boundary layer research*, G. E. A. Meier and K. Sreenivasan, eds., DLR, Springer, pp. 73–82.
- [99] Arnoldi, W. E., 1951. “The principle of minimized iterations in the solution of the matrix eigenvalue problem”. *Quart. Appl. Math.*, **9**, pp. 17–29.
- [100] Saad, Y., 1980. “Variations of arnoldi’s method for computing eigenelements of large unsymmetric matrices”. *Lin. Algebra. Appl.*, **34**, pp. 269–295.

Appendix: Spectral collocation method for spatial discretization of operators

The one-dimensional linear eigenvalue problems posed in this paper may be solved by constructing an operator that discretizes an n -th order linear ODE in the form

$$\mathcal{L}(\hat{y}) = a_n(\hat{y})D^{(n)} + \dots + a_1(\hat{y})D^{(1)} + a_0(\hat{y}) \quad (66)$$

where $D^{(m)}$ is the m -th derivative with respect to the independent variable x and a_0, a_1, \dots, a_n are functions of x . A collocation approach requires a discrete grid, x_i , and associated differentiation matrix, both of which are defined in the corresponding sections of this paper. For now, we keep the symbolic form

$$\mathcal{L}_{ij} = a_n(\hat{y}_i)D_{ij}^{(n)} + \dots + a_1(\hat{y}_i)D_{ij}^{(1)} + a_0(\hat{y}_i) \quad (67)$$

with $D_{ij}^{(m)}$ the m -th derivative matrix corresponding to the collocation points \hat{y}_i and a_0, a_1, \dots, a_n evaluated at \hat{y}_i . Here \mathcal{L}_{ij} denotes the contribution of grid point \hat{y}_j to the operator \mathcal{L} at \hat{y}_i .

When using spectral collocation methods, the value of a function $\phi(\hat{y})$ at a point \hat{y} can be obtained by using interpolant polynomials constructed for the dependent variables in terms of their values at the collocation points. Thus an N -th order polynomial can be represented as

$$\phi(\hat{y}) = \sum_{j=0}^N \Omega_j(\hat{y}) \tilde{\phi}(\hat{y}_j), \quad (68)$$

where the collocation points

$$\hat{y}_j = \cos \frac{\pi j}{N}; \quad j = 0, 1, \dots, N \quad (69)$$

are the extrema of the N -th order Chebyshev polynomial T_N defined on the interval $-1 \leq \hat{y}_j \leq 1$. The interpolant $\Omega_j(\hat{y})$ for the Chebyshev scheme is given as

$$\Omega_j(\hat{y}) = \left(\frac{1 - \hat{y}_j^2}{\hat{y} - \hat{y}_j} \right) \frac{T'_N(\hat{y})}{N^2 c_j} (-1)^{j+1}, \quad (70)$$

where

$$c_0 = c_N = 2 \quad \text{and} \quad c_j = 1, \quad 0 < j < N. \quad (71)$$

The derivatives of the function $\phi(\hat{y})$ can also be expressed in terms of its value at the collocation points. The collocation derivative matrix D for the Gauss-Lobatto grid is denoted by

$$D_{GL}^{(1)} \equiv (d_{ij}), \quad 0 \leq i, j \leq N \quad (72)$$

and the elements d are

$$\left. \begin{aligned} d_{00} &= -d_{NN} = \frac{(2N^2 + 1)}{6} \\ d_{jj} &= \frac{x_j}{2(x_j^2 - 1)}, \quad 1 \leq j \leq N-1 \\ d_{ij} &= \frac{c_i (-1)^{i-j}}{c_j (x_i - x_j)}, \quad i \neq j \end{aligned} \right\} \quad (73)$$

with c_j defined by (71). The general m -th collocation derivative matrix, can simply be found by

$$D^{(m)} \equiv D^m \quad (74)$$

It is rare that the domain on which a function we are interested in coincides with the standard domains on which the spectral grids are defined, although the much-studied Poiseuille flow in a straight channel is an exception, since we may normalize the normal-to-the-walls direction by the channel half-width so as to make the calculation grid coincide with the standard Chebyshev domain. If a mapping function $y = y(\hat{y})$ is used to map the domain of interest y onto the standard collocation domain \hat{y}_j , the collocation derivative matrices are modified by use of the chain rule as

$$\widehat{D}_{kj}^{(1)}(y) = \frac{d\hat{y}}{dy} D_{kj}^{(1)}(\hat{y}) \quad (75)$$

$$\widehat{D}_{kj}^{(2)}(y) = \left(\frac{d\hat{y}}{dy}\right)^2 D_{kj}^{(2)}(\hat{y}) + \frac{d^2\hat{y}}{dy^2} D_{kj}^{(1)}(\hat{y}) \quad (76)$$

$$\begin{aligned} \widehat{D}_{kj}^{(3)}(y) &= \left(\frac{d\hat{y}}{dy}\right)^3 D_{kj}^{(3)}(\hat{y}) + 3\frac{d^2\hat{y}}{dy^2}\frac{d\hat{y}}{dy} D_{kj}^{(2)}(\hat{y}) \\ &\quad + \frac{d^3\hat{y}}{dy^3} D_{kj}^{(1)}(\hat{y}) \end{aligned} \quad (77)$$

$$\begin{aligned} \widehat{D}_{kj}^{(4)}(y) &= \left(\frac{d\hat{y}}{dy}\right)^4 D_{kj}^{(4)}(\hat{y}) + 6\frac{d^2\hat{y}}{dy^2}\left(\frac{d\hat{y}}{dy}\right)^2 D_{kj}^{(3)}(\hat{y}) \\ &\quad + 3\left(\frac{d^2\hat{y}}{dy^2}\right)^2 D_{kj}^{(2)}(\hat{y}) + 4\frac{d^3\hat{y}}{dy^3}\frac{d\hat{y}}{dy} D_{kj}^{(2)}(\hat{y}) \\ &\quad + \frac{d^4\hat{y}}{dy^4} D_{kj}^{(1)}(\hat{y}). \end{aligned} \quad (78)$$